JGR Earth Surface

RESEARCH ARTICLE
10.1029/2019JF005355

Key Points:
- The ecosystem-type approach is applied to simulate permafrost dynamics on the Seward Peninsula
- Improved regional scale model is used to simulate snow interception and scouring
- Enhanced model calibration approach is implemented to allow for better use of historical borehole data

Supporting Information:
- Supporting Information S1

Correspondence to:
M. V. Debolskiy,
mvdebolskiy@alaska.edu

Citation:
Debolskiy, M. V., Nicolsky, D. J., Hock, R., & Romanovsky, V. E. (2020). Modeling present and future permafrost distribution at the Seward Peninsula, Alaska. *Journal of Geophysical Research: Earth Surface*, *125*, e2019JF005355. https://doi.org/10.1029/2019JF005355

Received 4 SEP 2019
Accepted 10 JUN 2020
Accepted article online 26 JUN 2020

©2020. American Geophysical Union. All Rights Reserved.

Modeling Present and Future Permafrost Distribution at the Seward Peninsula, Alaska

M. V. Debolskiy[1], D. J. Nicolsky[1], R. Hock[1], and V. E. Romanovsky[1,2,3]

[1]Geophysical Institute, University of Alaska Fairbanks, Fairbanks, AK, USA, [2]Earth Cryosphere Institute, Siberian Branch of the Russian Academy of Sciences, Tyumen, Russia, [3]Department of Cryosophy, Tyumen State University, Tyumen, Russia

Abstract Permafrost, a key component of Arctic ecosystems, is currently affected by climate warming and anticipated to undergo further significant changes in this century. The most pronounced changes are expected to occur in the transition zone between the discontinuous and continuous types of permafrost. We apply a transient temperature dynamic model to investigate the spatiotemporal evolution of permafrost conditions on the Seward Peninsula, Alaska—a region currently characterized by continuous permafrost in its northern part and discontinuous permafrost in the south. We calibrate model parameters using a variational data assimilation technique exploiting historical ground temperature measurements collected across the study area. The model is then evaluated with a separate control set of the ground temperature data. Calibrated model parameters are distributed across the domain according to ecosystem types. The forcing applied to our model consists of historic monthly temperature and precipitation data and climate projections based on the Representative Concentration Pathway (RCP) 4.5 and 8.5 scenarios. Simulated near-surface permafrost extent for the 2000–2010 decade agrees well with existing permafrost maps and previous Alaska-wide modeling studies. Future projections suggest a significant increase (3.0°C under RCP 4.5 and 4.4°C under RCP 8.5 at the 2 m depth) in mean decadal ground temperature on average for the peninsula for the 2090–2100 decade when compared to the period of 2000–2010. Widespread degradation of the near-surface permafrost is projected to reduce its extent at the end of the 21st century to only 43% of the peninsula's area under RCP 4.5 and 8% under RCP 8.5.

1. Introduction

Permafrost, the ground material at or below 0°C for two or more consecutive years, occurs widely in the Arctic and constitutes an important component of the global climate system. Among many physical processes controlled by permafrost, the permafrost-carbon cycle dynamics (Schuur et al., 2015) and hydrological cycle (Walvoord & Kurylyk, 2016; Woo et al., 2008) are among the top few influencing global climate dynamics. As the ground temperature responds to climate warming (Romanovsky, Smith, et al., 2010; Romanovsky et al., 2019), degradation of the near-surface permafrost asserts short- and long-term disturbances to vegetation (Burn & Friele, 1989; Cray & Pollard, 2015; Jorgenson et al., 2013; Schuur & Mack, 2018) and defines stability of infrastructure (Shiklomanov et al., 2017). For decades, the permafrost distribution and ground temperatures have been extensively studied on a wide range of spatial and temporal scales (Romanovsky & Osterkamp, 1995; Romanovsky, Drozdov, et al., 2010; Romanovsky, Smith, et al., 2010). Numerical modeling of ground temperature dynamics (Riseborough et al., 2008) has been widely used to fill in spatial and temporal gaps between observations and then project ground temperature conditions into the future (e.g., Gisnås et al., 2013; Nicolsky et al., 2017).

This study focuses on the Seward Peninsula located along the western coast of Alaska, just south of the Arctic Circle (see Figure 1). The Seward Peninsula also contains a transition zone between continuous and discontinuous permafrost (Jorgenson et al., 2008). This zone is of particular concern since changes in the ground temperature and permafrost-controlled processes are expected to be most pronounced in this zone (Lawrence et al., 2008). The peninsula was studied as part of the Arctic Transitions in the Land-Atmosphere System (ATLAS) Project (Walker et al., 2003) whose goal was to investigate tundra ecosystems in a warming climate. Other studies were focused on vegetation (Vavrek et al., 1999), hydrology (Hinzman et al., 2003), and permafrost (Hinzman et al., 2005). Findings from these studies reveal that the permafrost within the Seward Peninsula is predominantly associated with tundra vegetation, that is,

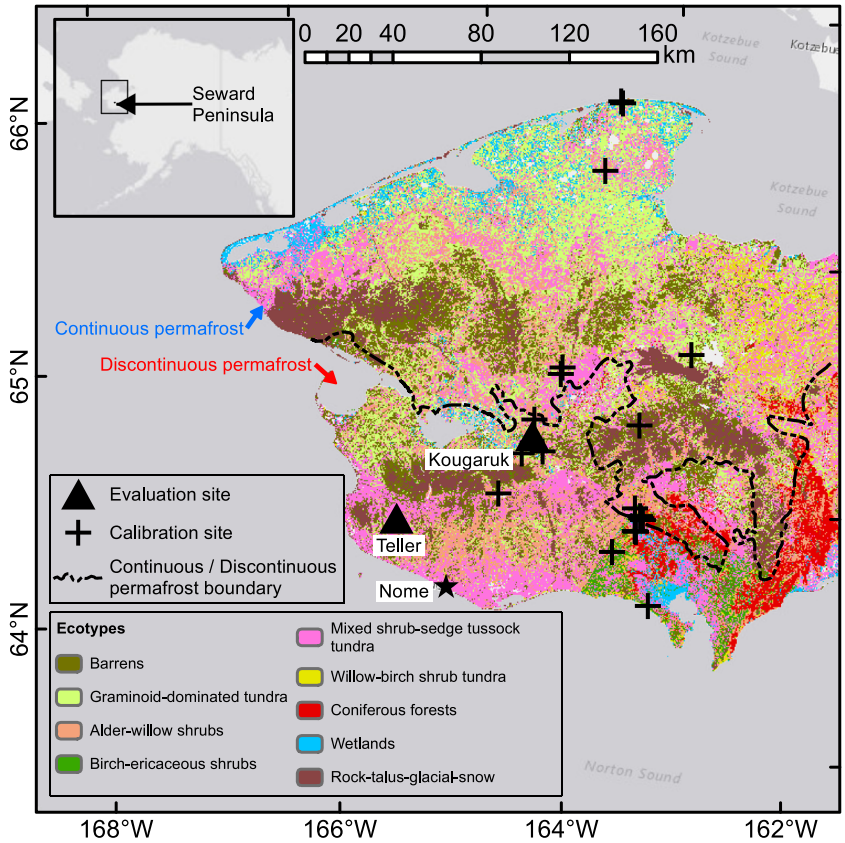

Figure 1. Map of the study area showing the ecotype distribution across the Seward Peninsula as well as the locations of stations used for the model calibration and evaluation. Each model evaluation site includes 8 to 10 boreholes located in the distinct ecotypes. The black dashed line delineates zones of the continuous (north) and discontinuous (south) permafrost distribution (Jorgenson et al., 2008). The small inset illustrates the spatial location of the Seward Peninsula with respect to the Alaska.

dwarf shrubs, lichens, and with barren land hilltops that experience significant snow redistribution (Walker et al., 2003). A layer of perennially unfrozen ground material between seasonally frozen ground and permafrost has typically been found under tall shrubs and forests. To further investigate permafrost dynamics, ground temperature observations were established at several sites in the Seward Peninsula in the early 2000s (Walker et al., 2003); most of them are used in this study for model calibration (Figure 1).

In general, subsurface temperature fields can be simulated by statistical-empirical or numerical models (Riseborough et al., 2008). The former models are usually represented as a regression approach and are used to determine a probability of the frozen/unfrozen state under certain conditions (Lewkowicz & Ednie, 2004; Panda et al., 2010; Pastick et al., 2015). Although statistical models are relatively robust, they lack modeling of the permafrost's thermal inertia and could not be easily adapted to simulate the talik formation and its consequent dynamics.

In this study, we use a direct numerical modeling approach that deterministically estimates the subsurface temperature at a particular point in time and depth by solving relevant equations. Numerical models are usually divided into equilibrium (e.g., Riseborough, 2010) and transient (e.g., Gisnås et al., 2013; Nicolsky et al., 2007) classes depending on whether or not thermal equilibrium is assumed (Riseborough et al., 2008). The peninsula's ground temperature and permafrost dynamics have been investigated as part of deterministic regional (Busey et al., 2005) and Alaska-wide (Jafarov et al., 2012; Marchenko et al., 2008) modeling efforts. However, these studies have been performed neither with a high spatial resolution nor with the assimilation of all publicly available data.

Here, we use the distributed transient temperature dynamic model called GIPL2 (Nicolsky et al., 2017), where GIPL2 stands for the Geophysical Institute Permafrost Lab model, Version 2. We enhance GIPL2 by

introducing an additional parameter to account for the snow interception by vegetation and scouring by wind. The GIPL2 model is then parameterized by utilizing historical borehole temperature data and a new calibration algorithm. The model parameters are distributed across the domain according to ecosystem-type classification. Consequently, the model is evaluated for fitness using temperature records collected within the ongoing Next-Generation Ecosystem Experiment project (https://ngee-arctic.ornl.gov/). After evaluating the model performance, we simulate ground temperature dynamics across the entire peninsula with a resolution of 500 m for the period 1901–2100. For hindcast modeling, we use the Climate Research Unit (CRU) monthly global data (Harris & Jones, 2017), while for the future projections, we employ two Representative Concentration Pathway (RCP) 4.5 and 8.5 scenarios (Meinshausen et al., 2011; Moss et al., 2008).

2. Study Area

The Seward Peninsula is approximately 330 km long and 145 km wide, with a mean elevation of approximately 150 m above the sea level. Four mountain ranges stretch along the southern side of the peninsula with the highest peak reaching 1,437 m above sea level. The mean annual air temperature of −2.6°C and mean annual precipitation of 430 mm are recorded in the largest settlement on the southern coast, Nome, over the period 1970–2000. Kotzebue, the closest meteorological station north of the Seward Peninsula, records mean annual air temperature of −5.2°C and an annual precipitation of 280 mm for the same period. A seasonal snow typically lasts from October to May (Cherry et al., 2017) with the climatological mean of the maximum snow depth varying between 0.5 and 0.7 m (Cherry et al., 2019). The northern part of the peninsula is dominated by continuous permafrost, which is associated with tussock tundra and wet bogs, while the southern parts feature discontinuous permafrost and forests (see Figure 1 for the ecotype distribution across the peninsula). Permafrost also occurs on rocky hilltops with barren or sparse vegetation.

Permafrost-related research on the peninsula has a long history; for example, Jones et al. (2011), Jones et al. (2012), and Yoshikawa and Hinzman (2003) studied thermokarst lake evolution; Lloyd et al. (2003) and Rupp et al. (2001) explored connections between the permafrost and vegetation dynamics; and Höfle et al. (1998) focused on the permafrost affected soils. In addition, other research focused on responses of permafrost and overlaying vegetation to fires (Liljedahl et al., 2007; Racine et al., 2004; Rupp et al., 2001). Previous research, however, has not included the regional assessments of ground temperature dynamics with high resolution. In the next section, we introduce our approach to modeling permafrost on the Seward Peninsula with a resolution of 500 m, which could be further increased to the resolution of existing ecotype maps, that is, 30 m if necessary. For the sake of computational efforts, we present the results only on the 500 m grid resolution.

3. Model Description

To simulate ground temperature dynamics, we use a spatially distributed GIPL2 model, which solves a nonlinear heat equation with phase change (Carslaw & Jaeger, 1959). Similar to other permafrost modeling studies (e.g., Gisnås et al., 2013; Westermann et al., 2015; Wu et al., 2018), GIPL2 assumes no water movement and no sources or sinks of heat. Vertical heat diffusion is assumed to dominate over lateral heat fluxes. Under these assumptions, subsurface temperature dynamics in snow and ground material is governed by the 1-D nonlinear heat equation:

$$C\frac{\partial T}{\partial t}+L\eta\frac{\partial \theta}{\partial t}=\frac{\partial}{\partial z}\left(k\frac{\partial T}{\partial z}\right),\qquad t\geq 0,\quad z_b\leq z\leq z_s, \tag{1}$$

where T is temperature, t is time, z is the vertical coordinate, η is porosity, $0<\theta<1$ is the unfrozen liquid water pore fraction, L is the volumetric latent heat of fusion, C is the volumetric heat capacity, and k is thermal conductivity. For the ground material ($z_b\leq z\leq 0$), we assume that $C=C_f(1-\theta)+C_t\theta$ and $k=k_f^{1-\theta}k_t^{\theta}$ (De Vries & Van Wijk, 1963; Sass et al., 1971). Here, the subscripts "f" and "t" denote frozen and thawed states, respectively. Thermal properties C and k for the snowpack ($0\leq z\leq z_b$) are parameterized according to Verseghy (1991) and Yen (1981), respectively. To describe multiple horizons such as an organic soil, mineral soil, and bedrock, several vertical layers with distinct parameters are considered. Typical values are listed in Table 1. Equation 1 is supplemented by a set of initial and boundary conditions. The lower boundary

Table 1
List of Model Parameters and Their Typical Range of Variability, as Found in the Literature

Symbol	Parameter name	Units	Typical range	Calibrated range
η	Soil porosity	m^3/m^3	0.05–1	0.07–0.79
k_f	Thermal conductivity, frozen soil	W/m^2	0.05–4	0.58–2.76
k_t	Thermal conductivity, thawed soil	W/m^2	0.05–4	0.05–2.37
C_f	Volumetric heat capacity, frozen soil	kJ/m^3	1,500–3,200	1,600–2,700
C_t	Volumetric heat capacity, thawed soil	kJ/m^3	1,500–3,200	1,900–3,000
ϱ_{ws}	Density of the snow wind slab	kg/m^3	10–800	100–460
α	Snow catchment coefficient	m/m	0–5	0.1–2.3

Note. The calibrated range indicates a spread of model parameters across all considered ecotypes after the calibration procedure.

condition ($z = z_b$) is determined by the geothermal heat flux. At the upper boundary ($z = z_s$), the air temperature T_a and precipitation P control the surface temperature and define the depth z_s of snow, if present, respectively.

We enhance the GIPL2 model used to study the tundra environments (Nicolsky et al., 2017) by adding an additional model parameter α to account for snow interception by vegetation or snow reduction by wind scouring, for example, on hill tops:

$$P_{\text{snow}} = \alpha P, \quad \text{when } T_a < 0^\circ\text{C}, \tag{2}$$

where P_{snow} is the solid precipitation available for snow accumulation (Nicolsky et al., 2017) and P is the solid precipitation from the forcing data set. Inclusion of α into GIPL2 allows us to account for the snow scouring ($\alpha \in [0,1]$) on the hill tops and extra accumulation ($\alpha > 1$) by shrubs. This new parameter provides a simpler, empirical way to describe wind-induced snow redistribution as discussed by Liston et al. (2016) and references therein. The snow cover redistribution was also discussed in the Cryogrid 1 model (Gisnås et al., 2013) in the framework of the so-called N-factor approach (Riseborough et al., 2008) for snow. However, no direct modeling of temperature in the snowpack was conducted. In the updated GIPL2 model, we incorporate α as an adjustment to the solid precipitation that is applied prior to calculation of the heat transfer both in the snow and ground material. Another snow-related parameter in GIPL2 that is calibrated in this study is ρ_{ws}—initial density of the wind slab layers. Since ρ_{ws} depends on wind speed and is a priori unknown, we estimate it for different ecosystem types during calibration. Further details about GIPL2 and its recent development can be found in Jafarov et al. (2012) and Nicolsky et al. (2017).

While most permafrost models (e.g., Gisnås et al., 2013; Jafarov et al., 2012; Marchenko et al., 2008; Rawlins et al., 2013; Volodin, 2008) determine the model parameters as a function of overlaying vegetation, soil type, and bedrock, in this study, we calibrate the model parameters for distinctive spatial units with similar vegetation and soil conditions. These units are commonly referred to as ecosystem types or ecotypes. The ecosystem-type approach assumes a strong link between climate, surface vegetation type, and subsurface substrate. This idea was first introduced by Humboldt (1806) and further developed with the focus on Alaska by Jorgenson and Kreig (1988) and Viereck (1970). In the context of ground temperature modeling, this link allows to use vegetation as a proxy for thermal properties of the ground material and snow parameters. This approach allows us to obtain a unique set of model parameters for each ecotype and to account for spatial heterogeneity. This method was successfully implemented in previous studies modeling permafrost in Alaska and Canada by Cable et al. (2016), Zhang et al. (2013), and Nicolsky et al. (2017).

Although many permafrost-vegetation feedbacks are bidirectional (e.g., Jorgenson & Kreig, 1988; Shur & Jorgenson, 2007; Viereck, 1970), in this work, we only assume unidirectional influence of the vegetation on permafrost. Thus, following the ecosystem-type approach, we classify the study area into nine ecotypes listed in Table 2 (written communications with Amy Breen, UAF, 2019) by connecting the Circum Arctic Vegetation Map from Walker et al. (2005) and the Circum Boreal Vegetation Map (Talbot & Meades, 2011) to the 30 m resolution Alaska Existing Vegetation Type (AKEVT) map (Fleming, 2015). The latter is based on the vegetation classification developed for Alaska by Viereck et al. (1992). The general Level 1 CAVM/CBVM vegetation types are used as a proxy for the ecotypes unless they can be divided into subtypes that can be distinguished by both different vegetation and difference in ground temperature regime from

Table 2
Ecotype Classification Used for Distributing Model Parameters Across the Seward Peninsula

Ecotype	Vegetation class	Coverage area (%) Continuous zone	Discontinues zone	Entire peninsula	*N*
1. Barrens	Dryas/lichen dwarf shrub tundra, foliose, and fruticose lichen-ridge	13.6	14.5	13.9	2
2. Graminoid-dominated tundra	Bluejoint-shrub-herb, tussock/lichen tundra, mesic sedge-grass-herb meadow-tundra, and sedge-willow-dryas tundra	29.9	13.9	24.2	2
3. Alder-willow shrubs	Alder-willow shrub	11.3	17.8	13.7	2
4. Birch-ericaceous shrubs	Birch-ericaceous shrub	0.2	4.0	1.6	3
5. Mixed shrub-sedge tussock	Mixed shrub-sedge tussock tundra-bog tundra	21.2	27.0	23.3	5
6. Willow-birch shrub tundra	Willow shrub, birch-willow shrub, and willow-sedge shrub tundra	4.0	2.8	3.5	1
7. Coniferous forests	White spruce forest and black spruce with lichen moss forest	1.6	8.0	3.9	1
8. Wetlands	Sweetgale-graminoid bog, wet meadow tundra, wet sedge-grass meadow-marsh, wet sedge bog-meadow, halophytic wet meadow, and aquatic herbaceous	5.7	3.0	4.7	2
9. Rock-talus-glacial-snow	Snow-ice, rock-talus-glacial, and sand-gravel-mud	9.6	6.7	8.5	1
10. Water	Water	2.9	2.3	2.7	—

Note. Composition of vegetation classes from Fleming (2015) for each ecotype, relative spatial coverage within the permafrost extent zones (Jorgenson et al., 2008) and entire peninsula, and the number *N* of existing boreholes related to the ecotype in the calibration procedure.

historical borehole data. Thus, barrens, graminoid-dominated tundra, wetlands, and coniferous forests are based on Level 1 CAVM/CBVM vegetation types. Alder-willow shrubs, birch-ericaceous shrubs, mixed shrub-sedge tussock tundra types, and willow-birch shrub tundra divide erect shrub-dominated tundra types and Level 1 vegetation type into four ecotypes based on the observed ground temperature and metadata of the 11 boreholes used for calibration. Areas that are assigned the nonvegetated type in CAVM/CBVM classification are separated into areas under the water table and others since there are no boreholes under the water bodies and cells assigned to the "water" type are not included into the computations. The final ecotype map with 500 m resolution is obtained by majority resampling of the 30 m resolution map. The use of CAVM/CABM Level 1 classification is also motivated by the potential use of calibrated model parameters for pan-Arctic modeling studies.

4. Model Application

We simulate ground temperature dynamics on a 500 m resolution grid covering the entire Seward Peninsula for the period from 1901 to 2100. We initialize simulations in September 1901 to assure a proper spin-up of the model. The soil column is extended down to the depth of 200 m. Temperature within the seasonally thawed or seasonally frozen layer is calculated using an equilibrium permafrost model (Romanovsky & Osterkamp, 1995; Sazonova & Romanovsky, 2003). Below the seasonal freeze/thaw layer, the temperature is assumed to increase according to the geothermal heat flux at the lower boundary of 0.085 W/m^2 (Davies, 2013), which is assumed constant in time and across the peninsula.

To define the upper boundary conditions, we use a 2 km resolution monthly air temperature and precipitation data sets developed by Scenarios Network for Alaska Planning (SNAP, 2017). In particular, the monthly temperature and precipitation time series for the period of 1901–2016 are obtained from the global CRU product (Harris & Jones, 2017) and then are downscaled to a 2 km grid using the Parameter-elevation Relationships on Independent Slopes Model (PRISM) climate mapping system (Daly et al., 2002). The latter uses a weighted regression scheme to account for topography and other factors. For the future climate projections (2006–2100), we exploit a composite average of the monthly air temperature and precipitation from five Global Circulation Models (GCMs) that optimally perform for Alaska (Walsh et al., 2008). The future climate projections are based on the RCP 4.5 and 8.5 scenarios (IPCC, 2013; Meinshausen et al., 2011). The GCM outputs are debiased by the delta approach and then downscaled in the same way as the CRU data (SNAP, 2017). To develop a smooth transition between the historical and projected data, we implement a

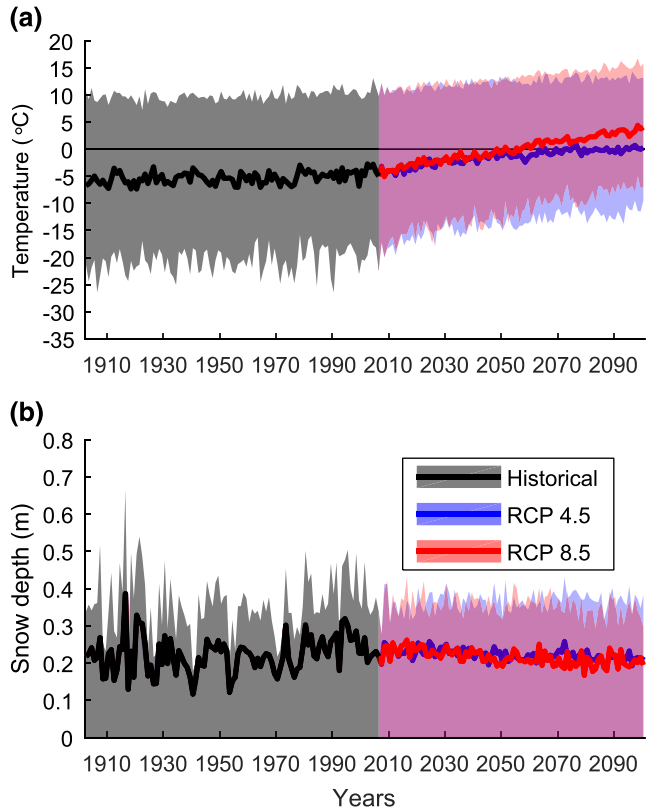

Figure 2. Spatially averaged dynamics of (a) the air temperature and (b) the snow depth across the Seward Peninsula. Solid lines show the mean annual temperature and mean winter snow depth, respectively. Shaded areas show a range of the spatially averaged monthly variability.

linear weight function for the period of overlap (2006–2016). The near-surface air temperature on the 2 km grid, while interpolated to a 500 m grid, was adjusted according to the constant lapse rate of 0.9°C per 100 m of elevation difference between the 2 km and 500 m digital elevation models (DEMs). The DEM for the 2 km grid is available at SNAP (2017), while elevations for the 500 m grid are extracted from the ecotype map package (Fleming, 2015). Precipitation is interpolated by the nearest neighbor method (MathWorks, 2018).

The mean annual air temperature averaged across the study area and its monthly variability are shown in Figure 2a. We note that the RCP 4.5 and 8.5 scenarios result in a 4°C and 7°C increase in the mean annual air temperature by the 2090s relative to the 2000s, respectively. The snow depth, shown in Figure 2b, does not exhibit any significant long-term trend with respect to the historical forcing. The increase in air temperature is thought to be a main driver for the ground temperature warming and the subsequent permafrost degradation.

5. Model Calibration

In order to simulate the present and future ground temperature within the study domain, values of the model parameters need to be estimated. The goal of model calibration is to establish a unique set of parameters for each ecotype so that the simulated ground temperatures represent measured ground temperature data.

5.1. Calibration Procedure

We calibrate soil-related (η, k_f, and k_t) and snow-related (α and ϱ_{ws}) parameters; ranges of their variability are listed in Table 1. Two additional soil parameters (C_f and C_t) are not included into the calibration algorithm, since the model is found to be not sensitive to these parameters on timescales exceeding several weeks (Nicolsky et al., 2017). Values C_f and C_t are taken from literature and available references (e.g., Hinzman et al., 1991; Osterkamp & Romanovsky, 1996; Romanovsky & Osterkamp, 1995). Similarly, we do not estimate the parameterization of the unfrozen liquid water content but rather take a typical dependence from, for example, Nicolsky et al. (2017). Characteristics of the particular dependencies for every ecotype are prescribed to soil layers based on the borehole logs and soil pit information. Since we assume five soil layers in the soil column, the total number of parameters to be calibrated per ecotype is 17 (three per each soil layer and two for the snow). Layer depths and remaining noncalibrated soil properties are determined from a visual inspection of photographs of soil pits or from borehole core descriptions.

Our objective is to find model properties for each ecotype (recall that there are nine distinct ecotypes; see Table 2) using ground temperature data from 19 shallow boreholes. We emphasize that some ecotypes have more than one borehole associated with it. The number N of boreholes associated with the ecotype is listed in the last column of Table 2. For these ecotypes, the found model parameters need to reflect data from all boreholes associated with the ecotype in some averaged sense.

The boreholes were drilled by the University of Alaska Fairbanks, U.S. Geological Survey, and National Park Service in various locations on the Peninsula (see Figure 1 for their locations). The boreholes are up to 3 m deep and have up to eight (typically five) sensors. All boreholes were equipped with data loggers with a sampling interval ranging from 1 hr to 1 day. Ground temperatures, snow height, air temperature, and surface temperature, if available, are aggregated to monthly means. The data cover a period from 1999 to 2014; however, no individual borehole covers the entire period and data gaps are present.

Similar to Nicolsky et al. (2007), parameters are estimated in two steps: First, we estimate parameters α and ϱ_{ws} by minimizing discrepancy simultaneously between simulated and observed snow depth and ground surface temperature at the borehole sites. This step is done separately since α and ϱ_{ws} are the only model

parameters that affect simulated snow depth. To estimate the remaining model parameters, we modify the variational data assimilation algorithm by Nicolsky et al. (2009) that utilizes available ground temperature, air temperature, and snow depth data. The algorithm is based on a nonlinear minimization of the cost function:

$$J(m) = \sum_{i=1}^{n} \left(\frac{1}{\Delta T_i^2} \left\| T^{(i)}(m) - T_o^{(i)} \right\|^2 \right) + \frac{1}{\Delta m^2} \|m - m_o\|^2, \tag{3}$$

where the measure of discrepancy $\|\cdot\|$ is defined below, m is the vector (in our case it has 15 elements) with model parameters for the ground material, n is the total number of calibration stations within an ecotype, $T^{(i)}(m) = T(x_i, z, t; m)$ and $T_o^{(i)} = T(x_i, z, t)$ are simulated and observed ground temperatures at the ith station, respectively, and m_o is the reference parameter vector for a given ecotype. Index i refers to the station within the ecotype with x_i being a vector of station coordinates. The uncertainties ΔT_i and Δm depend on the confidence in the model forcing and the reference parameter vector m_o, respectively.

To estimate the first weight in (3), we calculate a mismatch between the air temperature that was used to force the model and the observed air temperature at the ith station as follows:

$$\Delta T_i^2 = \frac{1}{\tau_2 - \tau_1} \int_{\tau_1}^{\tau_2} \left(T_f^{(i)}(t) - T_a^{(i)}(t) \right)^2 dt, \tag{4}$$

where τ_1 to τ_2 is the period for which the data are available, and $T_f^{(i)}$ and $T_a^{(i)}$ are forcing and observed air temperatures at time t at ith station within an ecotype. This weighting allows to value those stations more for which the forcing air temperatures better match the observations. In practical applications, the above integral becomes a sum over the available temperature observations. In this study, we use a monthly time step.

The measure of discrepancy in (1) between the observed and simulated ground temperatures at the ith station is calculated by

$$\left\| T^{(i)}(m) - T_o^{(i)} \right\|^2 = \frac{1}{\tau_2 - \tau_1} \int_{\tau_1}^{\tau_2} w_1(t) \sum_{k=1}^{n_z} w_2(z_k) \left(T^{(i)}(x_i, z_k, t; m) - T_o^{(i)}(x_i, z_k, t) \right)^2 dt. \tag{5}$$

Index $k = 1, ..., n_z$ refers to the discrete depth z_k, where ground temperature observations are available. The weights w_1 and w_2 are associated with the time of the year and depths of observation. The former weight is added for the summer measurements to be valued more than the winter months, since in the present-day Arctic environment, the summer ground temperatures are close to 0°C because of the phase change processes during the summer and a discrepancy between simulated and observed ground temperatures needs to be enhanced to be on par with its counterparts for the winter months. By increasing the value of w_1 during the summer results that the cost function $J(m)$ becomes more sensitive to the model parameters η and k_t defining the simulated ground temperature dynamics during the summer months. The weight w_2 increases exponentially with depth and hence increases the contribution of the deeper measurements compared to the shallow ones since ground temperature from shallower depths is subjected to a discrepancy between model forcing and observed air temperature and processes not related to the heat diffusion.

The second term in (3) includes the distance $\|m - m_o\|^2$ between the reference m_0 and variable m parameter vectors. Recall that the vector m has 15 elements, for example, representing k_f, k_t, and η for five soil layers. The weight Δm^2 represents our confidence in the reference vector m_0 for the given ecotype. We note that we do not compute $\|m - m_o\|^2$ and Δm^2 separately but rather calculate their ratio as

$$\frac{1}{\Delta m^2} \left\| m - m_o \right\|^2 = \sum_{l=1}^{15} \frac{\left(m_l - m_{o,l} \right)^2}{\Delta m_l^2}. \tag{6}$$

Here, m_l stands for the lth element of the parameter vector m (e.g., a value of the thermal conductivity k_f for the second layer), and $m_{o,l}$ is the reference value for m_l (i.e., the reference value for k_f from the a priori knowledge). Finally, Δm_l is an uncertainty associated with our confidence in the reference value $m_{o,l}$; that

is, it represents expert knowledge obtained by examining available data for the site, previous works, literature and field book notes, photographs, any laboratory measurements of thermal properties from the sites with similar conditions, and so forth. For example, it is possible to incorporate into m_o an increase in the thermal conductivity with depth and the fact that typically for a mineral soil $k_f > k_t$. The weight Δm_t also includes penalties for violating petrophysical constrains.

The cost function $J(m)$ can be minimized with respect to m by a variety of algorithms depending on the available computational resources and time. In this study, we use an internal point algorithm for the simplicity of implementation (MathWorks, 2018). However, the effectiveness and choice of the minimization algorithm could be an interesting topic for further investigations.

5.2. Calibration Results

Simulated and observed temperature dynamics for the three sites associated with the birch-ericaceous shrub ecotype are shown in Figure 3. Similar comparisons for other ecotypes are presented in the supporting information.

We emphasize that a single-parameter vector for the birch-ericaceous shrub ecotype must be found by assimilating data from all three stations simultaneously. It is evident that the match between observed and simulated temperatures is better for the Mauze Gulch and Blueberry Hill sites than it is for Guy Rowe. However, it can be expected because of the various weights $1/\Delta T^2$ standing in front of the discrepancies $\|\dot{\|}$ associated with the individual stations in the cost function. If the observed air temperature recorded at the station significantly differs from the downscaled CRU forcing, then the mismatch between the observed and simulated ground temperatures at this station is valued less in the cost function. Indeed, a smaller weight $1/\Delta T^2$ is computed for the Guy Rowe station, since the discrepancy between T_f and T_a is higher at Guy Rowe than it is at the other two stations. We emphasize that if each site was calibrated individually, we would obtain a different set of optimal parameters for each site and a better fit between the observed and simulated ground temperatures. However, in this case, it is necessary to average a set of recovered optimal parameters in some way.

Comparison of the simulated and observed monthly mean temperature for all 18 boreholes across all nine ecotypes is shown in Figure 4a. The mean bias, computed as an average of differences between all observed and simulated monthly ground temperatures, is −0.1°C. The corresponding root-mean-square error (RMSE) is 1.8°C. Comparison for the deepest sensors at all stations is shown in Figure 4b; the mean bias and RMSE are 0.2°C and 1.2°C, respectively. Note that the variance in mismatch decreases with depth. This is attributed to the weighting in the cost function that applies greater weights to the deeper sensors (typically with the depth ranging from 0.4 to 3 m below the surface), which generally do not exhibit effects of the nonconductive heat transfer and some lateral heat fluxes as well.

The effects of adding the new model parameter α to the GIPL2 model are illustrated in Figure 5. Parameterization of the snow redistribution by wind results in distinct values of α for the ecotypes; computations without inclusion of the snow redistribution effects are simulated by model runs with $\alpha = 1$. Note the simulated snow height (circles) without the snow redistribution ($\alpha = 1$) for some ecotypes underestimates the observed snow depth (see Figure 5a). Observed ground surface temperatures are available for almost every station that was used in calibration, while observed snow heights are scarce (1,022 and 266 monthly values in total, respectively). RMSE for ground surface temperatures is greatly reduced by calibration (4.2°C for simulations with calibrated α vs. 6.9°C for $\alpha = 1$) (see Figure 5b). The inclusion of the wind redistribution effects and subsequent calibration of the associated parameters helps to improve the fit to observations; however, some outliers still exist.

6. Model Evaluation

To evaluate how well the developed model performs at locations different from the calibration sites, we use a separate set of ground temperature observations, which are distinct from those incorporated in the model calibration process. In contrast to Jafarov et al. (2012) and Nicolsky et al. (2017) who used observed maximum active layer thickness for the model evaluation, we evaluate the model performance by only using the ground temperature records. This allows us to check the model performance consistently since the statistical measures are the same for the calibration and evaluation. In particular, we use ground temperatures

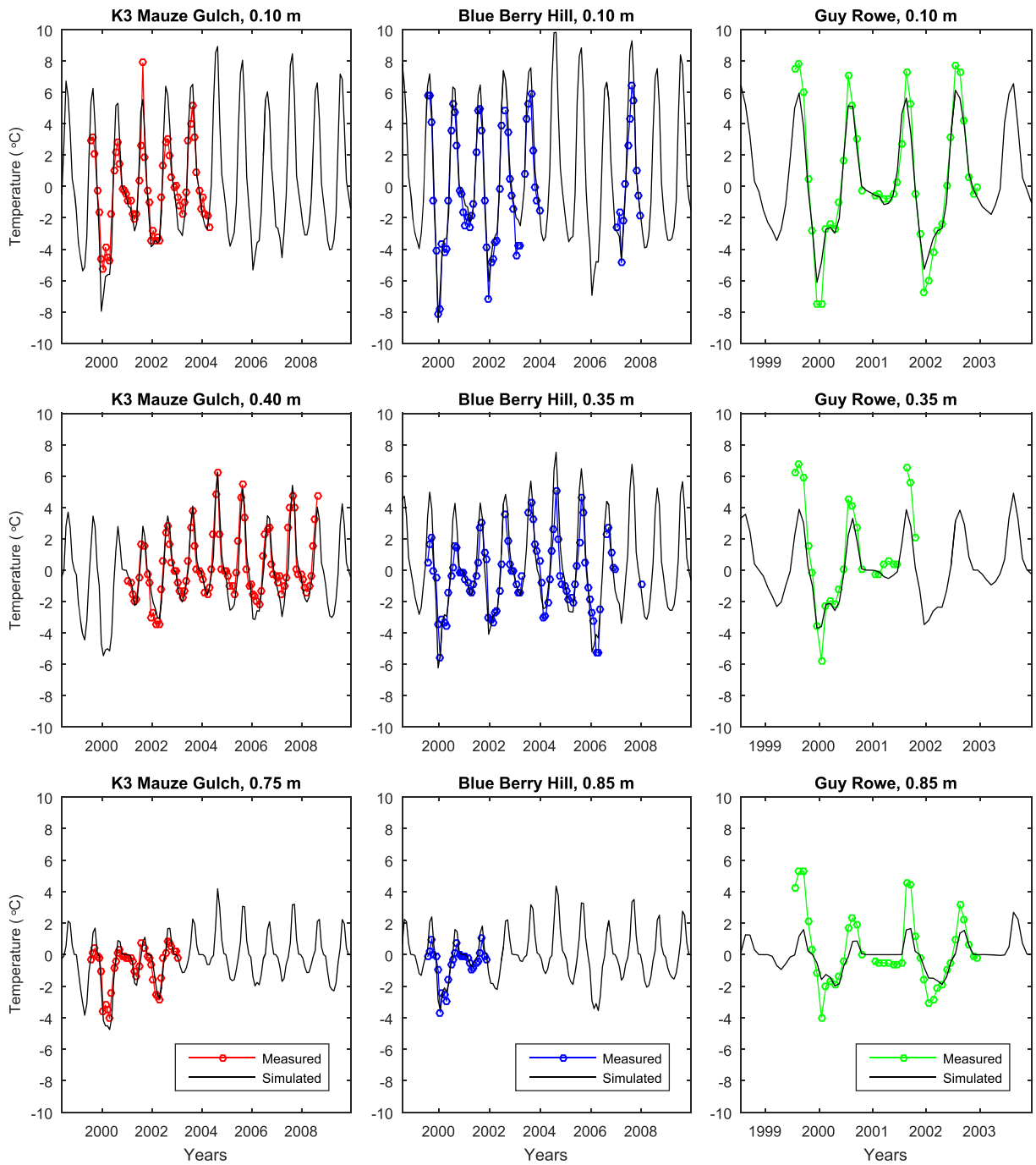

Figure 3. Comparison of the measured and simulated ground temperature dynamics at the different depths for three stations associated with the birch-ericaceous shrub ecotype.

collected at the Kougaruk and Teller sites (Figure 1). Each evaluation site contains 10 and 8 boreholes respectively situated in various ecotypes within a few kilometers distance from each other. Despite the proximity of boreholes within each evaluation site, these boreholes cover eight of the nine ecotypes with up to four boreholes per ecotype. The borehole data cover the peninsula-wide range of variability because of the heterogeneity at the local scale due to the diversity in vegetation cover, which is on par with the vegetation and climate variability across the peninsula. Finally, we note that the temperature sensors in the boreholes are located within the top 1.5 m and sample ground temperature hourly. Data from July

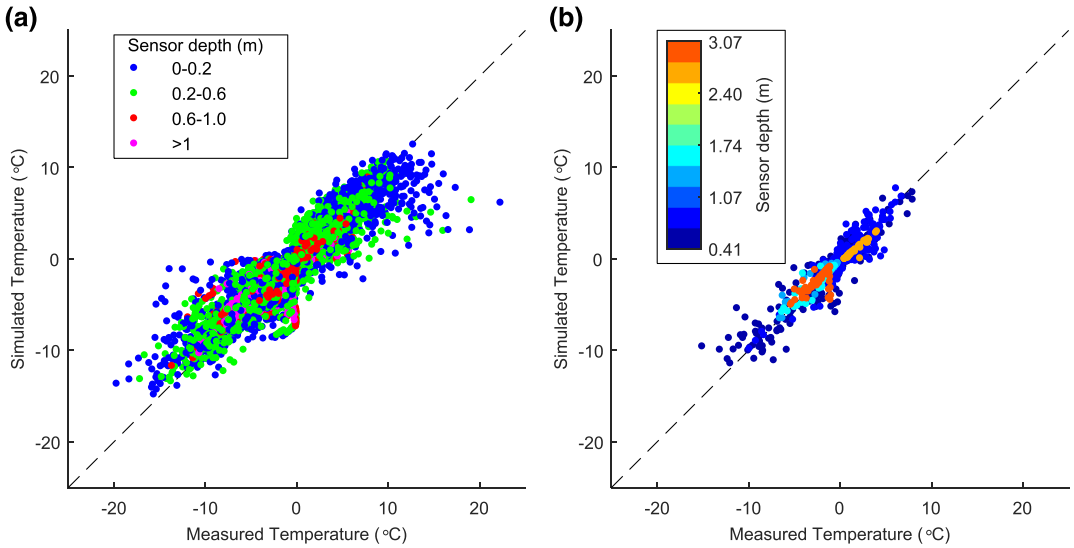

Figure 4. Comparison of the simulated and measured monthly mean ground temperatures at the calibration sites for (a) all sensors and (b) only the deepest sensor per station. The sensor depth is color coded.

2016 to July 2019 are used and aggregated into monthly means. Unfortunately, the coniferous forests do not exist at either the Kougarok or Teller site, and thus, this ecotype is excluded from the evaluation process.

To facilitate the evaluation study, the CRU data, both temperature and precipitation time series are used to provide the boundary conditions for the GIPL model through the early 2010s. The CRU data were then switched to the actual observed temperature and precipitation records (written communication, Robert Busey, 2020) for Kougaruk and Teller sites at 2012 and 2016, respectively. Observations from the nearby Kuzitrin River meteostation are used to fill in gaps in the temperature and precipitation time series for the Kougaruk site. Consequently, the GIPL model was used to simulate ground temperature at the evaluation sites through the observational period.

After analyzing borehole drilling records and assigning an ecotype for each borehole, we selected the corresponding sets of thermal properties for each borehole and then simulated temperature dynamics at the depths corresponding to the temperature sensors. Comparison of the simulated and observed ground temperature dynamics at boreholes associated with the birch-ericaceous shrub ecotype at Teller and Kougaruk is shown in Figure 6. Similar figures for other ecotypes can be found in the supporting information. Recall that the birch-ericaceous shrub ecotype was also used to illustrate the results of the calibration process (see Figure 3). Similarly to the calibration, the evaluation presents cases where the simulated temperature has some positive and negative biases with respect to the observations, across the stations associated with the same ecotype. However, the comparison between the simulated and observed temperatures is satisfactory during the entire period of measurements across all boreholes.

Next, we compare the simulated and observed monthly mean temperatures at all depths across all boreholes at the evaluation sites. Figure 7a shows the comparison at all depths, while Figure 7b displays the comparison at the deepest sensor at each borehole. Similar to the calibration process outcomes, the largest discrepancy occurs at the shallow sensors due to nonconductive heat transfer and possible frost heave of the sensors. Note that the ground temperature at the shallow sensors is very sensitive to the installation depth and can also experience most observational biases due to the frost heave action and nonconductive heat transfer. Despite some biases at the shallow depth, the simulated ground temperature agrees well with the observations.

A station at the top of the Kougaruk hill is located in the rock-talus environment and barely has any snow cover during the winter, resulting in the most significant discrepancy between the simulated and observed temperatures in both plots. Excluding this station, the overall model performance is comparable to the calibration results (Figure 4). The RMSE is 1.6°C, and the mean bias is −0.2°C for all data and 1.1°C and −0.1°C for the deepest sensors, respectively. The evaluation process demonstrates that the developed model performs well and can be used to simulate temperature across the entire study area.

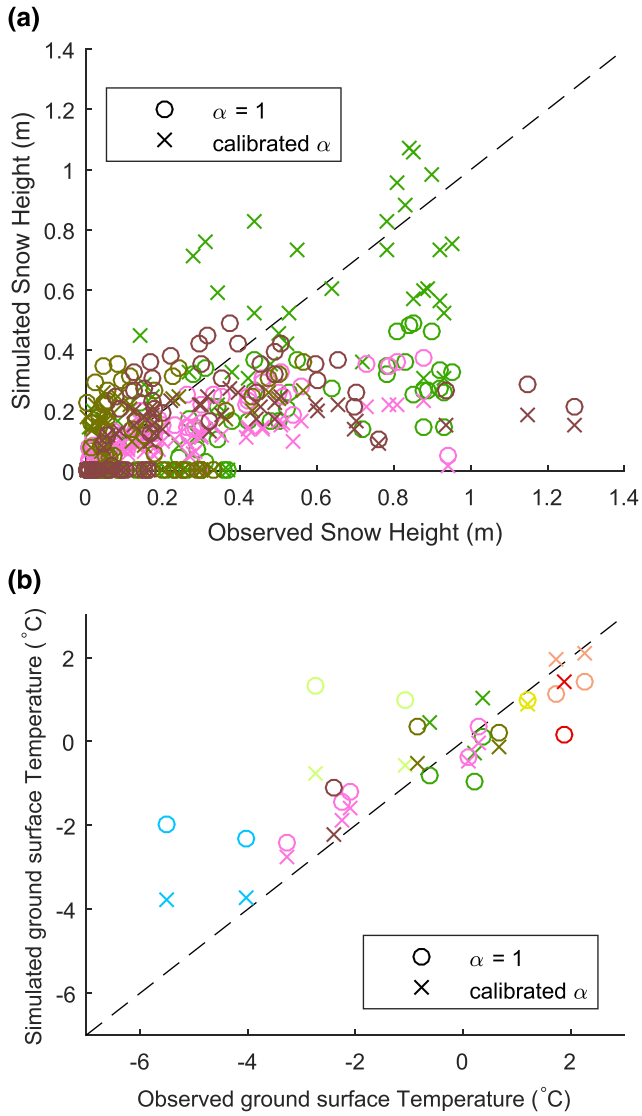

Figure 5. Comparison of the observed and simulated (a) monthly mean snow height and (b) mean ground surface temperature (averaged over all available months of observation) with (crosses) and without (equivalent to $\alpha = 1$, circles) including of the snow catchment coefficient α into the model. Colors indicate ecotypes as in Figure 1.

7. Results

We analyze simulated mean annual ground temperature at the 2 m depth, thickness of seasonally thawed and seasonally frozen layers, and talik thickness. A talik forms when the ground freezing in the winter stops reaching the permafrost table and a perennially unfrozen layer develops between the seasonally frozen layer and permafrost. Here, to avoid any confusion, we use terms such as "seasonally thawed layer" and "seasonally frozen layer" as defined by Yershov and Williams (1998) instead of the term "active layer," which is usually defined for areas with no talik above the permafrost table (Harris, French, et al., 1988). When no talik is present, the seasonally thawed layer (commonly known as an "active layer") exists above the permafrost during the summer and completely refreezes the following winter. When a talik is established, the seasonally frozen layer develops over the winter and completely thaws in the following summer. Maps of the simulated present (2000–2010) and future (2090–2100) distributions of the ground temperature, as well as seasonally thawed, seasonally frozen layers, and talik thicknesses, are presented in Figure 8. We use a decadal mean averaging to smooth the interannual variability in these parameters and to present a general direction of the ground temperature dynamics.

7.1. Present-Day Permafrost Conditions (2000–2010)

Our modeling results indicate that under the climate conditions in 2000–2010, the permafrost table is connected to the bottom of the seasonally thawed layer (i.e., no talik is present) across 84% of the Seward Peninsula area. In particular, no talik is present in 92% of the peninsula's continuous permafrost zone and in 70% of the discontinuous zone. Percentages of the permafrost coverage are listed in Table 3. The peninsula-averaged mean annual air temperature for the 2000–2010 decade is −3.6°C, and the air temperature is 1.2°C lower in the continuous permafrost zone than in the discontinuous zone. The mean annual ground temperature at the 2 m depth averaged for 2000–2010 reaches −2.5°C for the entire peninsula and is lower by 2°C in the continuous zone than in the discontinuous zone (Table 3). The present-day mean decadal seasonally thawed layer thickness is 1.1 m on average for the entire peninsula. Several-meter-thick taliks are present in the southern part of the peninsula. In addition, there are areas in the southern and southeastern part of the peninsula, where no near-surface permafrost has been present since the start of our simulations in 1901 (Figure 8). The present-day mean decadal seasonally frozen layer thickness in those areas and areas with recently developed taliks is 2.0 m on average.

Mean ground temperatures at the 2 m depth vary substantially between the different ecotypes, and the spatially averaged values with their standard deviations are listed in Table 4. The lowest ground temperatures occur at the nonvegetated hilltops (e.g., the rock-talus-glacial-snow ecotype), and the highest ground temperature is related to the alder-willow shrub and coniferous forest ecotypes. Barrens and mixed shrub-sedge tundra ecotypes demonstrate the highest spatial variability, whereas the lowest spread is found for the coniferous forest and birch-ericaceous shrub ecotypes. Overall, ecotypes that include shrubs (especially if they are tall) or forests have the highest ground temperatures. Areas with prevailing wet conditions in the northern part of the peninsula, hilltops, and slopes with almost no vegetation experience the lowest ground temperatures.

7.2. Permafrost Projections

Under the RCP 4.5 scenario, the mean decadal air temperature spatially averaged for the entire Seward Peninsula is projected to rise by 3.6°C in the last decade of the 21st century compared to the period 2000–2010 (see Table 3 for the details). The spatially averaged present-day air temperature increase differs

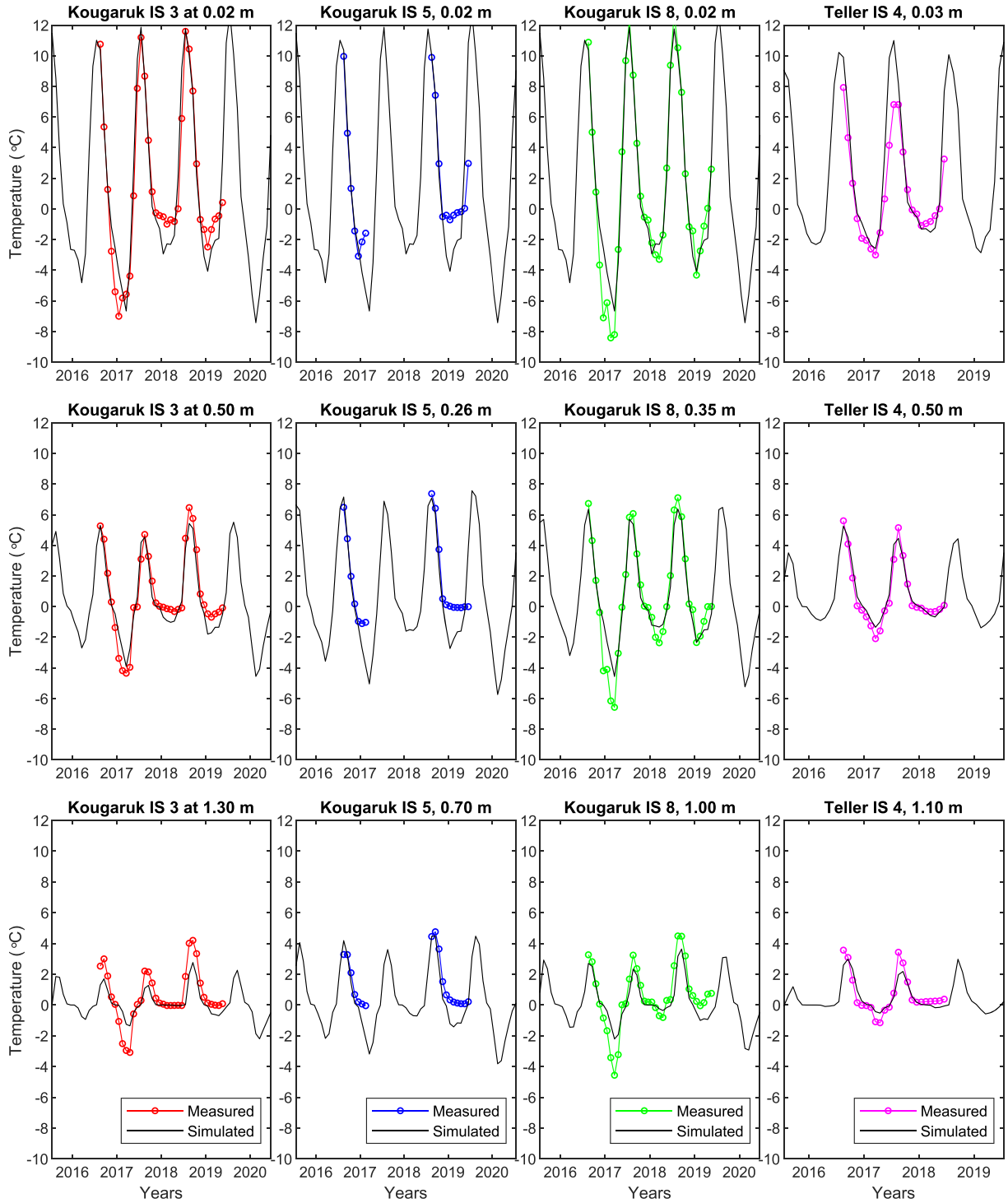

Figure 6. Comparison of the measured and simulated ground temperature dynamics at the evaluation sites for four stations associated with the birch-ericaceous shrub ecotype.

slightly by 0.1°C between the continuous and discontinuous permafrost zones. In response to this air temperature increase, the area underlain by the near-surface permafrost is projected to decrease by almost half of its present extent on the Seward Peninsula. Areas without taliks at the end of the 21st century decrease in the spatial coverage by 36% in the present-day continuous permafrost zone. In the present-day discontinuous permafrost zone, area without taliks, however, is decreased by more than 85% toward the

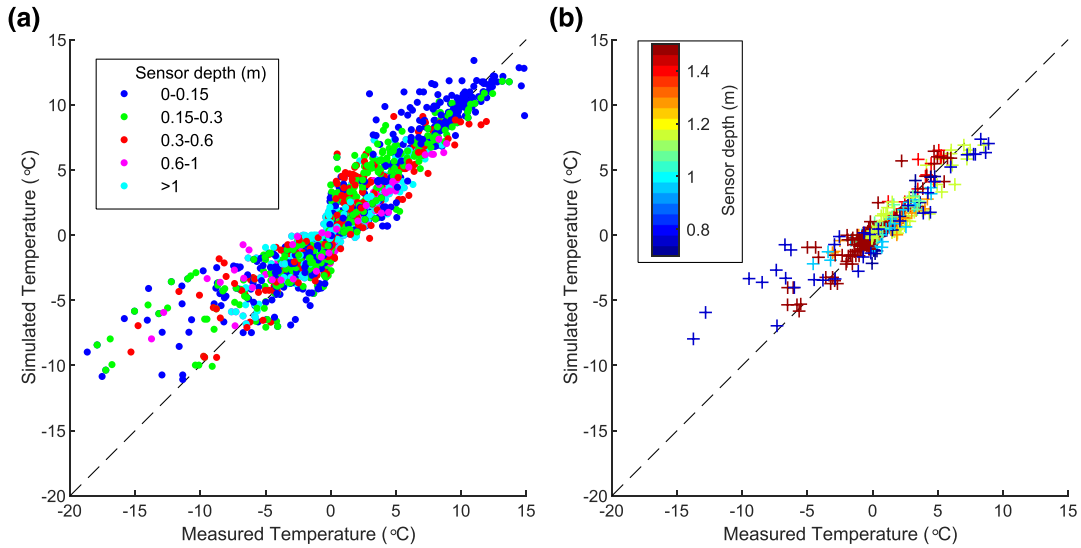

Figure 7. Comparison of the simulated and measured mean monthly ground temperatures at the evaluation sites for (a) all sensors and (b) only the deepest sensor per station. The sensor depth is color coded.

end of the century. The mean decadal ground temperature at the 2 m depth for the 2090–2100 decade becomes positive for the most of the peninsula, and its variability is decreased. The mean decadal seasonally thawed layer thickness spatially averaged across the entire peninsula is increased by 0.5 m, while seasonally frozen layer thickness is decreased by 1.5 m if compared to the 2000–2010 period.

Toward the end of the 21st century under the RCP 8.5 scenario, less than 1% of the Seward Peninsula experiences mean decadal air temperatures below 0°C in response to an average temperature increase by almost 7°C across the domain. As a result, near-surface permafrost may be present over only 8% of the entire peninsula. The ground temperature at 2 m depth for the last decade of the 21st century increases only by 4.4°C. The mean decadal seasonally thawed layer thickness for the entire peninsula may increase on average by 2.5 m if compared to the 2000–2010 decade. At the same time, in areas where taliks have been established before the beginning of the 21st century, the seasonally frozen layer thickness may decrease by 1.8 m on average for the entire peninsula.

Ground temperature dynamics throughout the whole modeling period (1901–2100) in continuous and discontinuous permafrost zones (Figure 9) suggest an overall two-century long warming trend. These figures illustrate a reduction in spatial spread when ground temperatures approach 0°C. The obvious difference in average values between the same ecotypes in different permafrost zones as well as the irregularities in the spatial spread are due to overall latitudinal air temperature gradient. It must also be noted that both permafrost zones have a different ecotype composition (Table 2) with different contributions from the same ecotype to zone-wide average ground temperature values and spatial spread.

The ground temperature response to the overall increase in air temperature across the Seward Peninsula in the 21st century is illustrated in Figure 10 and can be viewed in terms of the following three variables. First, $\Delta T_a = T_a|_{2090s} - T_a|_{2000s}$ stands for the difference between the mean decadal air temperature ($T_a|_{2090s}$) of the last decade of the century and its counterpart $T_a|_{2000s}$ for the first decade. Similarly, we define $\Delta T_s = T_s|_{2090s} - T_s|_{2000s}$ and $\Delta T_g = T_g|_{2090s} - T_g|_{2000s}$ as the differences between the mean decadal ground temperature for the last and first decades of the 21st century at the ground surface and 2 m depth, respectively. For both scenarios, the spatial variability in ΔT_a is lower than both the spatial variability in ΔT_s and ΔT_g. The latter could also be observed in Table 4. This illustrates that spatial heterogeneity of surface and soil conditions (ecotypes) amplifies the variability in ground temperature response at the surface and at the depth (see also Figure 9). In general, it can be expected that the increase in ground surface temperature should be different than the increase in air temperature ($\Delta T_s < \Delta T_a$) due to spatial and temporal variability in winter precipitation. This difference can also be a result of spatial and temporal variability in the amplitude of seasonal variations in air temperature. In particular, under the

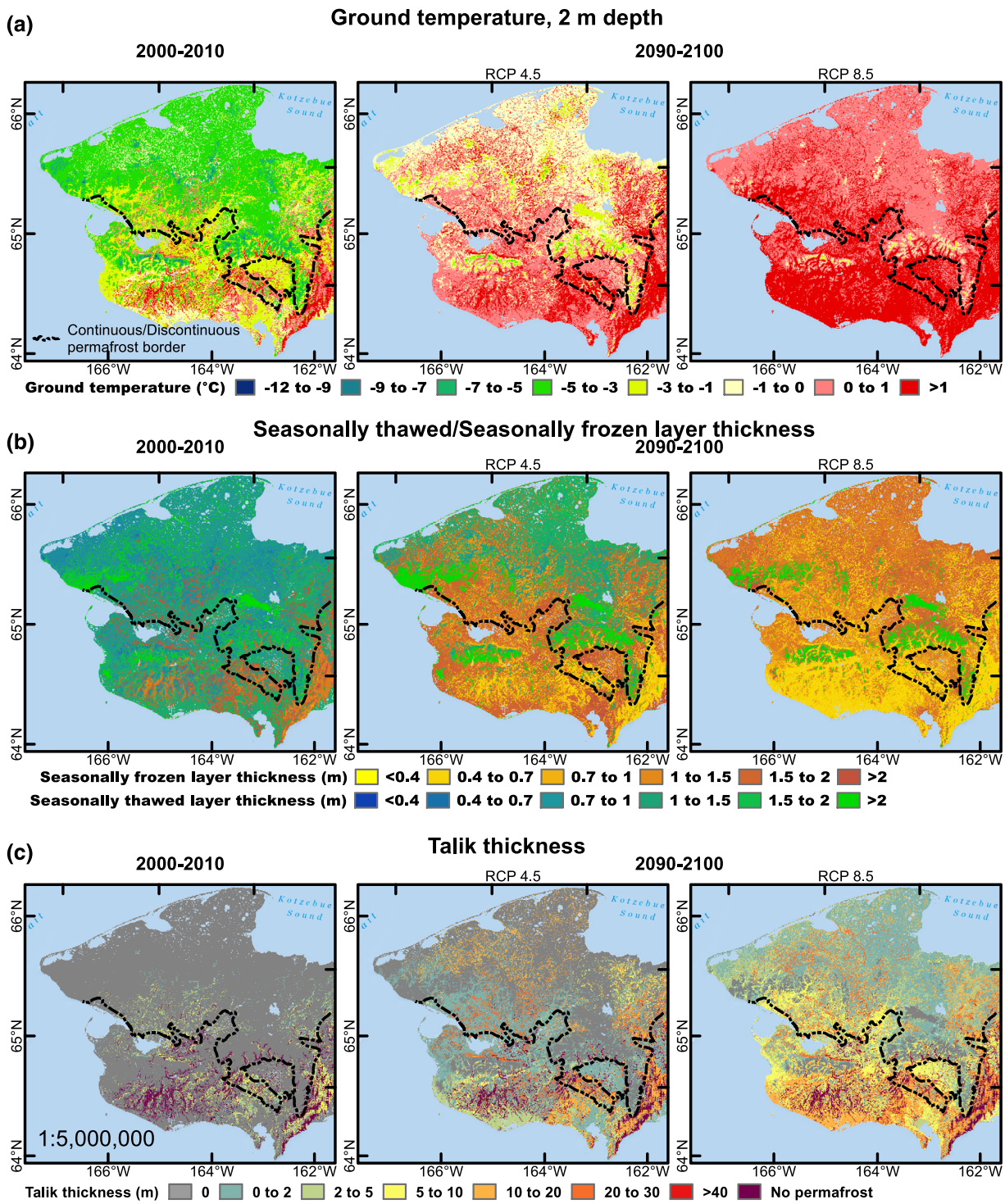

Figure 8. Decadal mean for (a) ground temperature at the 2 m depth, (b) seasonally thawed or seasonally frozen layer thickness, and (c) talik thickness across the Seward Peninsula during 2000–2010 and 2090–2100 for RCP 4.5 and 8.5 scenarios. The black line delineates zones of the continuous (north) and discontinuous (south) permafrost coverage from Jorgenson et al. (2008).

RCP 4.5 scenario, a substantial part of the peninsula (48%) shows larger ΔT_s than ΔT_a. For RCP 8.5, on the other hand, only on 8% of the peninsula ΔT_s is larger than ΔT_a. This difference suggests that an overall lower increase in air temperature can be amplified by the particular effects of heat transfer in the snow across large areas within the peninsula. Under a greater increase in temperature, snow starts

Table 3
Spatial Average and Standard Deviation of Mean Decadal Characteristics of the Permafrost Conditions and Ground Temperature Regime Across the Permafrost Extent Zones (Jorgenson et al., 2008) and the Entire Seward Peninsula

Domain	2000–2010	2090–2100 RCP 4.5	2090–2100 RCP 8.5	2000–2010	2090–2100 RCP 4.5	2090–2100 RCP 8.5
	Air temperature (°C)			Ground temperature, 2 m depth (°C)		
Continuous zone	−4.0±0.9	−0.4±0.9	3.0±0.9	−3.2±1.7	0.1±1.4	1.2±1.6
Discontinuous zone	−2.8±1.0	0.7±1.0	3.9±1.0	−1.2±1.8	1.1±1.6	2.9±1.8
Entire peninsula	−3.6±1.1	0.0±1.1	3.3±1.0	−2.5±2.0	0.5±1.5	1.9±1.9
	Permafrost extent (%)			Seasonally thawed layer thickness (m)		
Continuous zone	92	59	10	1.0±0.5	1.5±0.8[a]	3.6±0.4[a]
Discontinuous zone	70	10	3	1.2±0.4	2.2±1.1[a]	3.7±0.4[b]
Entire peninsula	84	43	8	1.1±0.5	1.6±0.8[c]	3.6±0.4[a]
	Talik extent (%)			Seasonally frozen layer thickness (m)		
Continuous zone	8 (2)[b]	41	90	2.3±0.6	0.5±0.2[c]	0.2±0.1[c]
Discontinuous zone	30 (8)[b]	90	97	1.8±0.5	0.5±0.3[c]	0.1±0.0[c]
Entire peninsula	16 (6)[b]	57	92	2.0±0.6	0.5±0.3[c]	0.2±0.1[c]

[a]Calculated only for areas with no taliks in 2090–2010. [b]Values in parentheses are for areas with no permafrost since the start of the simulations. [c]Calculated over areas with no permafrost or with taliks in 2000–2010.

to play a lesser role due to the decrease in the length of the period when snow is present. If we look at the areas where $\Delta T_g > \Delta T_a$, these areas comprise 25% and less than 1% for RCP 4.5 and 8.5, respectively. In widespread areas where the permafrost degradation has been initiated and the permafrost table starts to move downwards, the difference between ΔT_a (or ΔT_s) and ΔT_g depends on the gradient of the ground temperature above permafrost table. The discrepancy between the rate of air temperature increase and the rate at which permafrost table moves downwards results in overall larger $\Delta T_a - \Delta T_g$ over larger territory under RCP 8.5 compared to RCP 4.5. This is illustrated in Figure 10 where we depict the joint probability distributions $p(\Delta T_a, \Delta T_s)$ and $p(\Delta T_a, \Delta T_g)$ for each RCP. These probability distributions indicate how common are the specific ground temperature responses at the surface or at depth with respect to the increase in air temperature. It is equivalent to the relative frequency of occurrence of a specific combination of ΔT_s and ΔT_a (or ΔT_g and ΔT_a) on the peninsula. For RCP 8.5, a denser distribution can be observed for both ΔT_s and ΔT_g. It also must be noted that there are clear clusters with higher probabilities close to both the lower and upper limits of the overall range in ΔT_s for both RCPs. The joint probability distributions are formed from all of the grid cells within the study area where the ground temperature was simulated. The rectangles in Figure 10 are associated with the 95% spatial variability bounds for the considered scenarios and for different present-day permafrost distribution zones. The discontinuous permafrost zone shows an overall higher increase in both ΔT_s and ΔT_g variability compared to the continuous zone.

Table 4
Spatial Average and Standard Deviation of Mean Decadal Ground Temperature for Different Ecotypes Across the Modeling Domain

Ecotype	2000s	2090s RCP 4.5	2090s RCP 8.5
1. Barrens	−3.4±1.2	−0.1±0.4	1.0±1.0
2. Graminoid-dominated tundra	−3.9±0.8	−0.5±0.4	0.3±0.4
3. Alder-willow shrubs	0.6±0.9	3.3±0.6	4.8±0.5
4. Birch-ericaceous shrubs	−0.2±0.2	1.5±0.9	4.3±0.6
5. Mixed shrub-sedge tussock tundra	−2.4±1.2	0.1±0.3	1.8±1.4
6. Willow-birch shrub tundra	−1.0±0.9	1.8±0.8	3.9±0.7
7. Coniferous forests	0.8±0.4	3.2±0.4	4.8±0.4
8. Wetlands	−3.7±0.9	−0.3±0.3	0.4±0.3
9. Rock-talus-glacial-snow	−4.0±1.1	−1.2±0.9	0.7±1.1

Note. The temperature is provided at the 2 m depth.

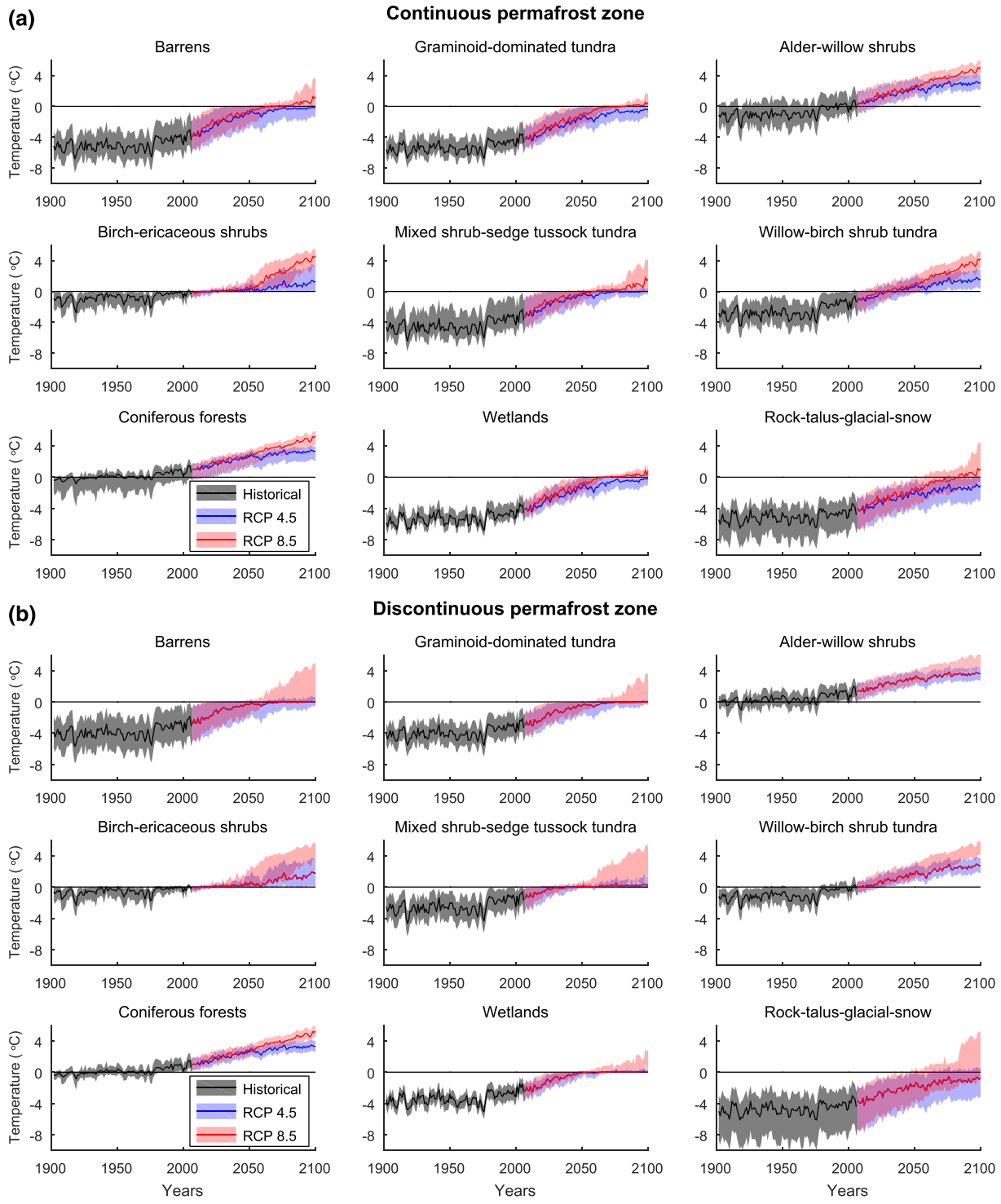

Figure 9. Simulated mean annual ground temperature at the 2 m depth over the period 1901–2100. Solid lines show spatial averages for the continuous (a) and discontinuous (b) permafrost zones. Shaded areas refer to the spatial 95% probability bounds across both zones.

8. Discussion

8.1. Uncertainties, Limitations, and Reliability of Projections

Generally, uncertainties in modeling of ground temperature dynamics arise from four sources: model physics, its numerical implementation; uncertainty in the model parameters; uncertainty of the boundary

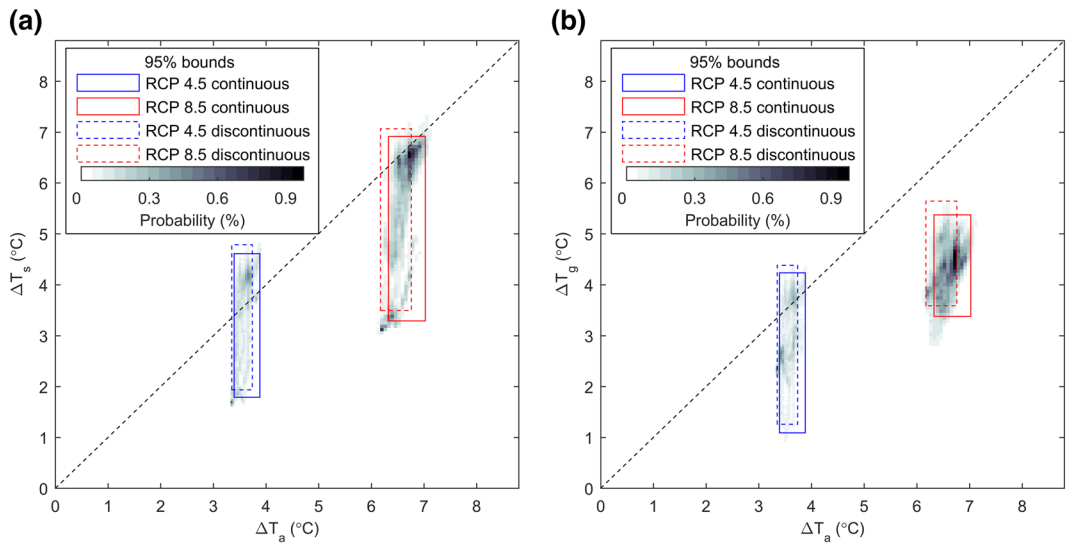

Figure 10. Comparison of differences ΔT_a, ΔT_s (a) and ΔT_g (b) in the mean decadal air, ground surface, and 2 m depth temperatures, respectively, for the 2090–2100 and 2000–2010 periods. Boxes show the 95% spatial variability bounds for the continuous and discontinuous permafrost zones for both RCP 4.5 and 8.5. Shading corresponds to joint probability distributions $p(\Delta T_a,\Delta T_s)$ (a) and $p(\Delta T_a,\Delta T_g)$ (b) for the considered RCP scenario.

conditions; and representation of auxiliary processes in the model. The uncertainties associated with the model physics and its numerical implementation are well described and quantified by Nicolsky et al. (2017). With regard to uncertainties originating from model parameters, in this application, we only add one additional model parameter α. The uncertainties and model sensitivity of other model parameters are described in Jafarov et al. (2012) and Nicolsky et al. (2017). The simple parameterization (2) allows us to account for additional snow interception by vegetation or for loss of snow by scouring. Ground temperatures are quite sensitive to the choice of this parameter, as shown in Figure 11. The sensitivity of ground temperature to change in α generally decreases with the depth in the soil. However, the decrease in sensitivity depends on the thermal properties of the soil. The uncertainty associated with the choice of parameter α in this application is reduced through the calibration process. By matching the simulated and observed snow depths as well as the ground surface temperatures, an optimal value of α is found for each ecotype. This allows to bring the uncertainty associated with the choice of parameter α closer to the uncertainty in snow depth and ground surface temperature data used in calibration.

To estimate the uncertainty from model parameters, we employ an ensemble approach. For each ecotype considered in this study, first, we run a Monte Carlo simulation for calibration station locations considering all 17 model parameters that were calibrated (α and ϱ_{ws} for snow and η, k_f, and k_t for each of the five soil layers). The simulations are performed on a sample of 1,000 parameter sets per ecotype. The values for parameters are drawn from uniform distributions within the typical ranges, listed in Table 1. From each simulation, we form a probability distribution of the cost function $J(m)$ (see the supporting information). Then we form a model ensemble that includes 100 parameter sets with the lowest cost function values per ecotype. The model ensembles for each ecotype are then run for the period 1901–2100 (both the RCP 4.5 and 8.5 scenarios) with three air temperature and precipitation variations within a scenario. These forcing variations for each emission scenarios are developed as follows: For each ecotype, air temperature and precipitation for each month are taken from the coldest and the hottest cell (in terms of air temperature) within the ecotype and a spatial mean air temperature and precipitation for the whole ecotype. The results of these ensemble runs are presented in Figure 12 (the supporting information also provides standard deviation and a full range of ground temperatures within the ensembles). Typical range of the ensemble for ground temperatures at 2 m is estimated to be from 1°C to 3°C and varies with ecotype. Maximum variability within the an ensemble is found for ensembles of alder-willow shrub, birch-ericaceous shrub, and coniferous forest ecotypes forced with the minimal air temperature and for the barrens, wetlands, and rock-talus-glacial-snow ecotypes forced with the maximal air temperature. The ground temperature variability within an

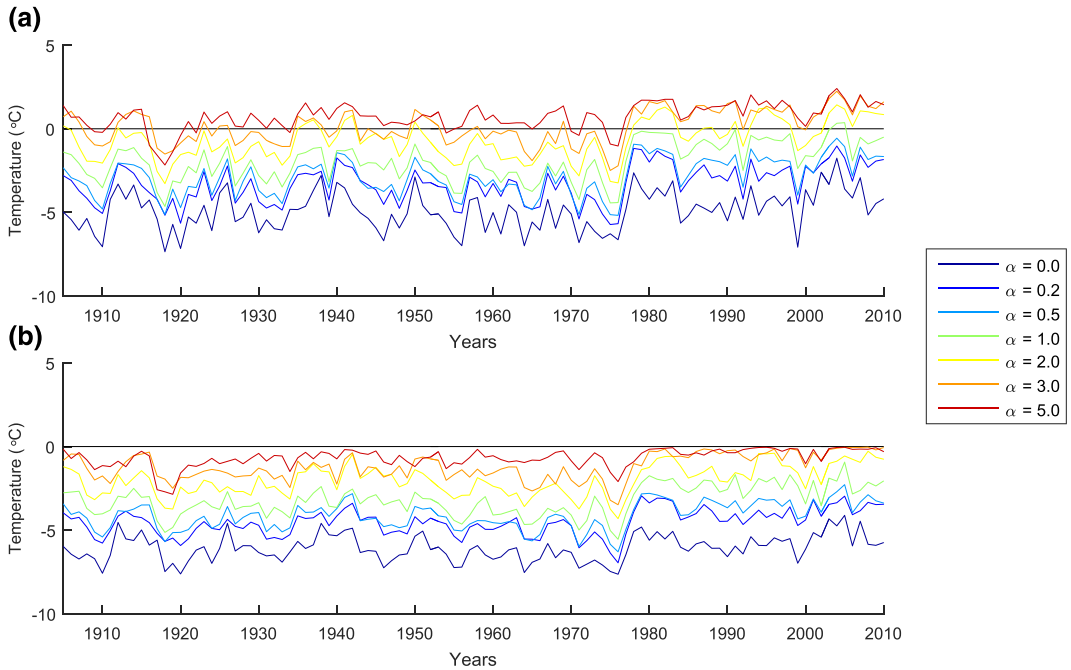

Figure 11. Sensitivity of the surface temperature (a) and ground temperature at 2 m depth (b) calculated for a station located in mixed shrub-sedge tussock tundra ecotype to the parameter α (calibrated value for this ecotype is 1.1).

ensemble is greatly reduced by 2–3°C when the forcing air temperature triggers permafrost degradation; however, the variability increases toward the end of the century. This is due to the fact that when permafrost degradation is initiated, a zero-curtain feature occurs within the ground temperature profile and the heat from the atmosphere is spent on melting the ground ice. The amount of the ground ice in soil is controlled only by η, and the rate of thawing front propagation is additionally affected by k_t. Thus, the ensemble variability in ground temperature at 2 m depth mostly depends on variability in those parameters during the period for which the zero curtain still exists at 2 m depth.

The uncertainty of the boundary conditions cannot be directly estimated for several reasons. For the upper boundary condition, the meteorological station data with long enough records that might be used for the comparison between the historical station data and the gridded climate product are already incorporated, both in the creation of the 0.5° by 0.5° CRU data set (Harris & Jones, 2017) and in downscaling (Daly et al., 2002). However, the calibration approach implemented in this study uses weighting that depends on the mismatch between the observed air temperature at calibration stations location and air temperature that is used as an upper boundary condition in GIPL2 (downscaled gridded data sets). Since the stations for which the forcing is closer to the observations are weighted higher, the effect of inadequate upper boundary condition to the choice of the optimal model parameter vector for any given ecotype is reduced. For the lower boundary condition, the estimated error in geothermal heat flux is 0.0415 W/m^2 (Davies, 2013). However, its contribution to the uncertainty in the simulated ground temperatures in the first 20 m can be assumed negligible (Alexeev et al., 2007; Lawrence et al., 2008).

Natural processes that may indirectly affect vertical soil heat transfer and thus ground temperatures, but are not explicitly presented in the model such as organic layer dynamics, water movement, and vegetation growth and succession, despite contributing to the uncertainty are beyond the scope of this study. However, some of that uncertainty is manifested in the data used for model calibration and evaluation. The similarity between statistical measures of mismatch between the simulated and observed ground temperatures for calibration and evaluation indicates that this uncertainty is partially accounted for in the calibration process. The proper estimation of the contribution of auxiliary processes to the total uncertainty of the ground temperature field is not possible since the model either lacks parameterizations for these processes or incorporates them implicitly in the model parameters through the calibration process. In either

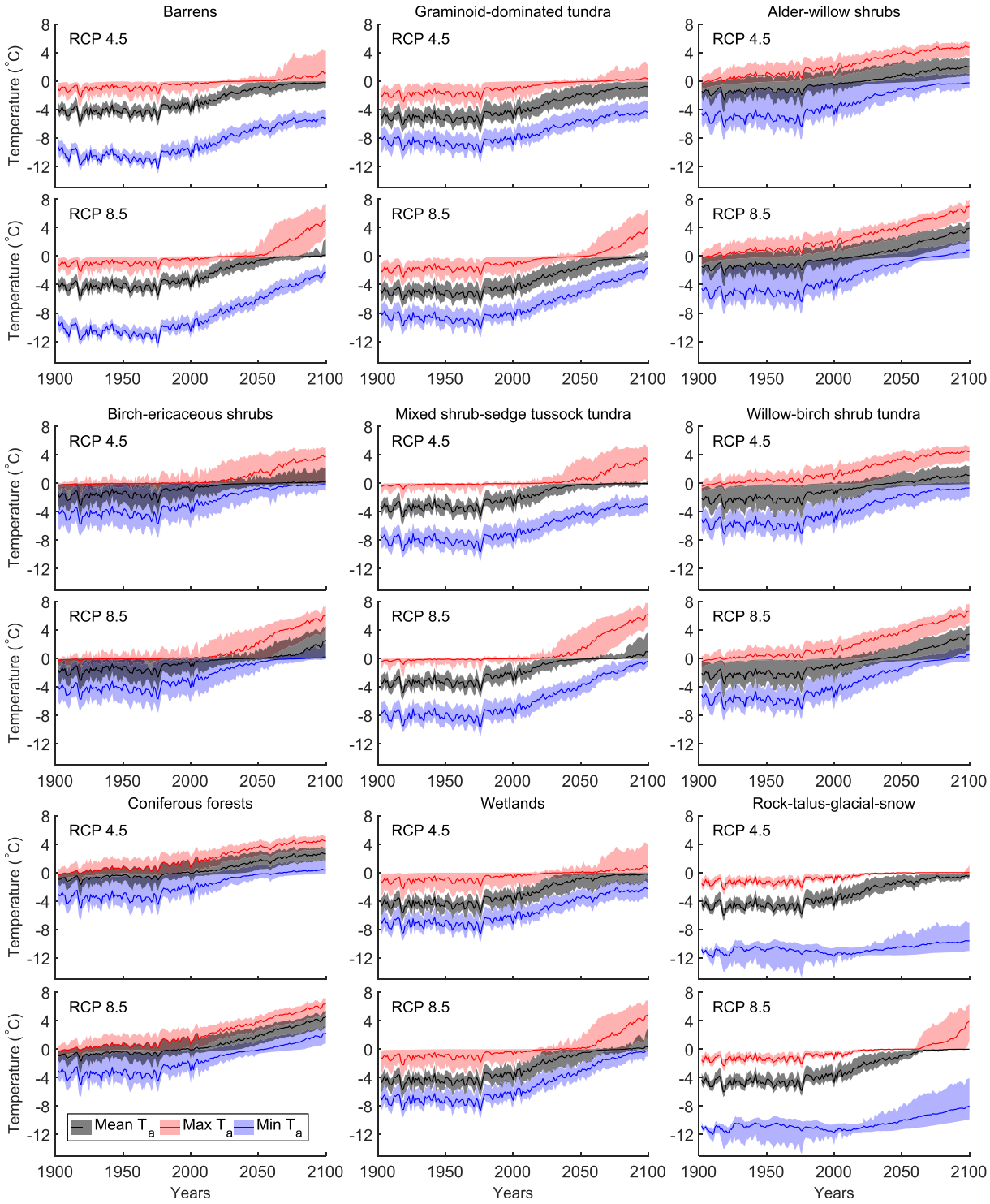

Figure 12. Ground temperature at 2 m depth for all ecotypes. Ensemble runs ($N = 100$) for each ecotype were forced with minimum (blue), mean (gray), and maximum (red) air temperature (T_a) within the study domain for a particular ecotype for both scenarios RCP 4.5 and RCP 8.5. Solid lines correspond to ensemble mean, and areas between minimum and maximum of the ensemble are shaded.

way, there is no clear direct path for the uncertainty propagation of this kind; however, small mean biases and RMSE especially for deeper soil layers in model evaluation suggest that the calibration approach implemented in this study provides reliable optimal model parameters and that the assumptions embedded in the model are reasonable.

The climate forcing is one of the primary controls of the ground temperature regime at shallow depths. Thus, the uncertainties and limitations inherent to the GCMs that provide climate forcing for future projections are imposed onto ground temperature projections in this study. Reliability of these projections directly depends on the probability of the emission scenarios that these projections are based on. Furthermore, other processes such as changes in vegetation cover due to climate change are not addressed in this study. The current ongoing increase in shrub cover extent (Myers-Smith et al., 2011), which is largely due to an increase in air temperature, is likely to continue in the future (Jorgenson et al., 2015). This will further contribute to the increase in ground temperatures since ecoptypes with shrubs intercept more snow (Table 2), thus increasing the ground surface temperature in the winter months. Therefore, the projections provided in this study can be described as conservative. Furthermore, to account for the processes mentioned above and to include permafrost-related feedbacks to the atmosphere, it would be necessary to use coupled atmosphere-snow-vegetation-soil model or an Earth system model, which is beyond the scope of this study.

The approach to modeling ground temperatures in this study has several limitations. The lateral spatial resolution is defined by the resolution of the boundary conditions data sets as well as the resolution of the ecotype map. On one hand, temporal resolution of the ground temperature dynamics is limited by the temporal resolution of the boundary conditions data sets. On the other hand, since the changes in the surface temperature are attenuated and lag with depth, the resulting ground temperature dynamics are usually aggregated on at least an annual timescale to provide any conclusive evidence of permafrost degradation or aggradation. To ensure proper estimation of the model parameters for each ecotype, at least one borehole temperature record per ecotype is required. The thicknesses and configuration of the soil layers for each ecotype require descriptions or photographs of the soil pits in proximity of these boreholes. The ecotype classification itself is limited by the total amount of available ground temperature data used for model parameter estimation for each ecotype and by the variability of surface and soil conditions these data represent. This limitation has manifested itself in the remaining mismatch between the observed and simulated ground temperatures in the calibration process, which could not be reduced any further by the data assimilation algorithm. The mismatch depends on the variability of the thermal properties within each ecotype, and an ecotype with a large mismatch may be better split into subtypes for calibration.

8.2. Comparison to Other Studies and Results Interpretation

Our results suggest higher ground temperatures in the south of the peninsula than those calculated by Jafarov et al. (2012) for 2000–2010. The discrepancy is most likely caused by different soil properties parameterization as well as by the different calibration approach. The parameter sets for the ecotypes in this study are specific to the Seward Peninsula, whereas in Jafarov et al. (2012), the soil parameters are calibrated for a broader domain. Nevertheless, the boundary between the discontinuous and continuous permafrost zones estimated here for the period 2000–2010 is in good agreement with Jorgenson et al. (2008). Near-surface permafrost coverage within discontinuous and continuous zones defined by Jorgenson et al. (2008) obtained in this study amounts to 70% and 92%, respectively, which agrees with permafrost extent zone definitions.

Another study (Marchenko et al., 2008) simulated mean ground temperatures at the 2 m depth for the peninsula in the year 2000 between −5.0°C and −2.5°C (according to the color gradation in Figure 3A in Marchenko et al., 2008), which at its upper end is comparable to the spatial average for the peninsula in this study, that is, −2.5°C. However, ground temperatures lower than −2.5°C are widespread in the north of the peninsula in this study. The difference between the values in the studies is most likely caused by the differences in spatial resolution (0.5° by 0.5° in Marchenko et al., 2008). Comparing the future projections is complicated since the emission scenarios and model forcing based on them in the previous studies are different from the ones utilized in this study. Finally, we note that we do not provide a comparison with the existing global permafrost modeling studies (e.g., Lawrence & Slater, 2005; Wang et al., 2019) since it is beyond the scope of this study. Furthermore, in most GCMs, the soil column is represented only by a few meters depth, which can overestimate temporal temperature variability (Alexeev et al., 2007). The presented results, if appropriately aggregated, could provide a benchmark for GCM ground temperature evaluations, since the presented simulations provide upscaling of the measured ground temperature across the study area.

Our modeling results suggest that under the present-day climate conditions, 84% of the Seward Peninsula is underlain by near-surface permafrost. However, near-surface permafrost will be present only on 43% and 8% of the peninsula at the end of the 21st century for RCP 4.5 and RCP 8.5, respectively. Near-surface permafrost

degradation and widespread formation of taliks will lead to the emergence of a perennially functioning suprapermafrost aquifer that will change runoff dynamics of the rivers and creeks on the Seward Peninsula. In addition, projected permafrost degradation will increase the occurrence of the thermokarst processes and together with the change of runoff dynamics will lead to changes in sediment and organic matter discharged to the ocean. Potential changes in carbon cycle across the peninsula due to widespread permafrost degradation are also to be expected. The estimation of these effects is out of the scope of this study; however, our results can be used to inform these estimations on a regional scale.

In terms of resilience of permafrost in different ecotypes to an increase in air temperature on a 100 year timescale, ecotypes with the lowest initial ground temperatures (barrens, graminoid-dominated tundra, wetlands, and rock-talus-glacial-snow) show the lowest ground temperatures at the end of the 21st century in both RCPs (Figure 9 and Table 4). Among those ecotypes, the amplitude of ground temperature increase is higher for ecotypes representing wetter conditions for RCP 4.5. However, in the case of higher air temperature increase (RCP 8.5), the ecotypes associated with dry hilltops (barrens and rock-talus-glacial-snow) experience a higher increase in ground temperature than the ecotypes with wetter surface conditions.

The narrowing of the spatial spread in mean annual ground temperatures of an ecotype when the spatial average of the mean annual ground temperature approaches 0°C from negative values (Figure 9) can be explained by the zero-curtain effect (Romanovsky, Smith, et al., 2010; Smith et al., 2005). This effect provides some temporal lag that allows for areas under lower than average air temperatures to catch up with the areas under higher air temperatures, given these areas belong to the same ecotype. This is also evident from Tables 3 and 4 where spatial standard deviations are smaller for average ground temperature values that are closer to 0°C. In addition to the zero-curtain effect, the rate at which the permafrost table lowers as the talik develops plays an important role in the response of soil temperatures to the increase in air temperature. Under RCP 8.5 within widespread areas with newly formed taliks (86% of the peninsula, Table 3), the permafrost table slowly lowers. The higher temperature gradients between the shallow permafrost table and the ground surface in areas with newly formed taliks result in overall larger differences between the increase in air and ground surface temperatures and in the ground temperature at 2 m depth under RCP 8.5 than under RCP 4.5 scenarios by the end of the 21st century (Figure 10 and Table 3).

9. Conclusions

In this study we expand the high-resolution ground temperature products developed earlier for the North Slope of Alaska (Nicolsky et al., 2017) to the Seward Peninsula. In addition, we added a model parameter to the snowpack submodel to account for different effects of vegetation on snow accumulation and redistribution and enhanced an existing data assimilation approach for a better model calibration, which is later verified by the model evaluation.

Modeling results for the present-day permafrost extent and temperature are generally in agreement with previous studies (Jafarov et al., 2012; Jorgenson et al., 2008; Marchenko et al., 2008) given the difference in the approaches, spatial scales, and climate data utilized. Substantial changes in permafrost are projected for the end of the 21st century. The whole peninsula experiences a steady increase in air temperatures under both RCP 4.5 and 8.5. For RCP 4.5 in the last decade of the 21st century in more than a half of the Seward Peninsula, the permafrost table will be disconnected from the seasonally freezing layer above it or permafrost will not be present at all. However, the areas occupied by more resilient ecotypes in the northern half of the peninsula will preserve near-surface permafrost under a seasonally thawed layer. Under a more extreme scenario RCP 8.5, in the last decade of the 21st century, less than 10% of the peninsula will have near-surface permafrost present.

The applicability of the modeling approach implemented in this study to other regions and different spatial resolutions depends on the availability of the high-resolution climate data, ground temperature observations available for calibration and evaluation of the model, and high-resolution ecotype classification maps. When ground temperature observations do not cover a sufficient number of ecotypes to adequately represent the variability of surface and subsurface conditions on a target resolution, two possibilities can be considered. Approximation of the model parameters for ecotypes where calibration data are absent by model parameters for the equivalent ecotype from an adjacent territory for which a calibration was already done should be

considered. If no equivalent ecotype can be found, planning and implementing a ground temperature data acquisition campaign should fill the necessary gaps.

Data Availability Statement

The simulated ground temperatures, auxiliary variables such as seasonally thawed, seasonally frozen layers, and talik thicknesses for 1901–2100 period with both emission scenarios for the 21st century, calibration and evaluation data, and ecosystem-type maps and classifications are available online (https://doi.org/10.5440/1579361) (Debolskiy et al., 2019).

Acknowledgments
We are grateful to Amy Breen (University of Alaska Fairbanks) for help in developing the ecosystem-type classification. We would like to thank Reginald Muskett (University of Alaska Fairbanks) and Santosh Panda (University of Alaska Fairbanks) for the preliminary processing of ground temperature data and maps. This research is funded by the National Science Foundation (NSF) Grants 1304271 and 1832238, by the Next-Generation Ecosystem Experiment (NGEE-Arctic) project, Alaska NSF EPSCoR Award 1757348, by the Russian Science Foundation (RSF) Grant RSF-16-17-00102, and by the state of Alaska. NGEE-Arctic is supported by the Office of Biological and Environmental Research in the DOE Office of Science.

References

Alexeev, V. A., Nicolsky, D. J., Romanovsky, V. E., & Lawrence, D. M. (2007). An evaluation of deep soil configurations in the CLM3 for improved representation of permafrost. *Geophysical Research Letters*, *34*, L09502. https://doi.org/10.1029/2007GL029536

Burn, C. R., & Friele, P. A. (1989). Geomorphology, vegetation succession, soil characteristics and permafrost in retrogressive thaw slumps near Mayo, Yukon Territory. *Arctic*, *42*(1), 31–40.

Busey, R., Hinzman, L., Yoshikawa, K., & Liston, G. (2005). *Simulating the permafrost distribution on the Seward Peninsula, Alaska*. Paper presented at AGU Fall Meeting Abstracts, 1105.

Cable, W. L., Romanovsky, V. E., & Jorgenson, M. T. (2016). Scaling-up permafrost thermal measurements in Western Alaska using an ecotype approach. *The Cryosphere*, *10*(5), 2517–2532.

Carslaw, H. S., & Jaeger, J. C. (1959). *Conduction of heat in solids*. London, UK: Oxford University Press.

Cherry, J., Jacobs, A., Heinrichs, T., Fisher, W., Delamere, J., Haase, C., et al. (2019). *Imiq hydroclimate database*. Fairbanks, Alaska: University of Alaska Fairbanks.

Cherry, J., Zhu, J., & Kirchner, P. (2017). *Snow cover monitoring with MODIS satellite data in Alaska's national parks, 2000–2015* (Natural Resource Report NPS/SWAN/NRR/2007/1566). Fort Collins, CO: National Park Service.

Cray, H. A., & Pollard, W. H. (2015). Vegetation recovery patterns following permafrost disturbance in a Low Arctic setting: Case study of Herschel Island, Yukon. *Arctic, Antarctic, and Alpine Research*, *47*(1), 99–113.

Daly, C., Gibson, W. P., Taylor, G. H., Johnson, G. L., & Pasteris, P. (2002). A knowledge-based approach to the statistical mapping of climate. *Climate Research*, *22*(2), 99–113.

Davies, J. H. (2013). Global map of solid Earth surface heat flow. *Geochemistry, Geophysics, Geosystems*, *14*, 4608–4622. https://doi.org/10.1002/ggge.20271

De Vries, D. A., & Van Wijk, W. R. (1963). Physics of plant environment. *Environmental control of plant growth*, *5*, 69.

Debolskiy, M. V., Nicolsky, D. J., Hock, R., & Romanovsky, V. E. (2019). *Modeling present and future permafrost distribution at the Seward Peninsula, Alaska: Modeling archive*. https://doi.org/10.5440/1579361

Fleming, M. D. (2015). *Develop an existing vegetation layer for the Western Alaska LCC region*. https://lccnetwork.org/resource/develop-existing-vegetation-layer-western-alaska-lcc-region

Gisnås, K., Farbrot, B. E. H., Schuler, T., & Westermann, S. (2013). CryoGRID 1.0: Permafrost distribution in Norway estimated by a spatial numerical model. *Permafrost and Periglacial Processes*, *24*(1), 2–19.

Höfle, C., Ping, C. L., & Kimble, J. M. (1998). Properties of permafrost soils on the northern Seward Peninsula, northwest Alaska. *Soil Science Society of America Journal*, *62*, 1629–1639.

Harris, S. A., French, H. M., Heginbottom, J. A., Johnston, G. H., Ladanyi, B., Sego, D. C., & van Everdingen, R. O. (1988). *Glossary of permafrost and related ground-ice terms* (pp. 1–142). Ottawa: Associate Committee on Geotechnical Research, National Research Council of Canada.

Harris, I., & Jones, P. (2017). *CRU TS4. 00: Climatic Research Unit (CRU) Time-Series (TS) version 4.00 of high-resolution gridded data of month-by-month variation in climate (Jan. 1901–Dec. 2015)* (pp. 1–25). Centre for Environmental Data Analysis.

Hinzman, L., Bettez, N. D., Bolton, W. R., Chapin, F. S., Dyurgerov, M. B., Fastie, C. L., et al. (2005). Evidence and implications of recent climate change in northern Alaska and other Arctic regions. *Climatic Change*, *72*(3), 251–298.

Hinzman, L., Kane, D., Gleck, R., & Everett, K. (1991). Hydrological and thermal properties of the active layer in the Alaskan Arctic. *Cold Regions Science and Technology*, *19*, 95–110.

Hinzman, L., Kane, D. L., Yoshikawa, K., Carr, A., Bolton, W. R., & Fraver, M. (2003). *Hydrological variations among watersheds with varying degrees of permafrost* (pp. 21–25). Paper presented at Proceedings of the Eighth International Conference on Permafrost.

Humboldt, A. (1806). *Ideen zu einer physiognomik der gewächse* (pp. 1–10). Leido en la Academia Real de Ciencias de Prusia el.

IPCC (2013). *Climate change 2013: The physical science basis. Contribution of Working Group I to the Fifth Assessment Report of the Intergovernmental Panel on Climate Change*. Cambridge, UK, and New York, NY: Cambridge University Press.

Jafarov, E. E., Marchenko, S. S., & Romanovsky, V. E. (2012). Numerical modeling of permafrost dynamics in Alaska using a high spatial resolution dataset. *The Cryosphere*, *6*(3), 613–624.

Jones, B. M., Grosse, G., Arp, C. D., Jones, M. C., Walter Anthony, K. M., & Romanovsky, V. E. (2011). Modern thermokarst lake dynamics in the continuous permafrost zone, northern Seward Peninsula, Alaska. *Journal of Geophysical Research*, *116*, G00M03. https://doi.org/10.1029/2011JG001666

Jones, M. C., Grosse, G., Jones, B. M., & Walter Anthony, K. (2012). Peat accumulation in drained thermokarst lake basins in continuous, ice-rich permafrost, northern Seward Peninsula, Alaska. *Journal of Geophysical Research*, *117*, G00M07. https://doi.org/10.1029/2011JG001766

Jorgenson, M. T., Harden, J., Kanevskiy, M., O'Donnell, J., Wickland, K., Ewing, S., et al. (2013). Reorganization of vegetation, hydrology and soil carbon after permafrost degradation across heterogeneous boreal landscapes. *Environmental Research Letters*, *8*, 35017.

Jorgenson, M. T., & Kreig, R. A. (1988). A model for mapping permafrost distribution based on landscape component maps and climatic variables. In Senneset (Ed.), *Proceedings of the Fifth International Conference on Permafrost* (Vol. 1, pp. 176–183). Trondheim, Norway: TAPIR Publishers.

Jorgenson, M. T., Marcot, B. G., Swanson, D. K., Jorgenson, J. C., & DeGange, A. R. (2015). Projected changes in diverse ecosystems from climate warming and biophysical drivers in northwest Alaska. *Climatic Change*, *130*(2), 131–144.

Jorgenson, M. T., Yoshikawa, K., Kanevskiy, M., Shur, Y., Romanovsky, V., Marchenko, S., et al. (2008). Permafrost characteristics of Alaska, *Proceedings of the Ninth International Conference on Permafrost* (Vol. 3, pp. 121–122). University of Alaska Fairbanks.

Lawrence, D. M., & Slater, A. G. (2005). A projection of severe near-surface permafrost degradation during the 21st century. *Geophysical Research Letters*, *32*, L24401. https://doi.org/10.1029/2005GL025080

Lawrence, D. M., Slater, A. G., Romanovsky, V. E., & Nicolsky, D. J. (2008). Sensitivity of a model projection of near-surface permafrost degradation to soil column depth and representation of soil organic matter. *Journal of Geophysical Research*, *113*, F02011. https://doi.org/10.1029/2007JF000883

Lewkowicz, A. G., & Ednie, M. (2004). Probability mapping of mountain permafrost using the BTS method, Wolf Creek, Yukon Territory, Canada. *Permafrost and Periglacial Processes*, *15*(1), 67–80.

Liljedahl, A., Hinzman, L., Busey, R., & Yoshikawa, K. (2007). Physical short-term changes after a tussock tundra fire, Seward Peninsula, Alaska. *Journal of Geophysical Research*, *112*, F02S07. https://doi.org/10.1029/2006JF000554

Liston, G. E., Perham, C. J., Shideler, R. T., & Cheuvront, A. N. (2016). Modeling snowdrift habitat for polar bear dens. *Ecological Modelling*, *320*, 114–134.

Lloyd, A. H., Yoshikawa, K., Fastie, C. L., Hinzman, L. D., & Fraver, M. (2003). Effects of permafrost degradation on woody vegetation at Arctic treeline on the Seward Peninsula, Alaska. *Permafrost and Periglacial Processes*, *14*(2), 93–101.

Marchenko, S., Romanovsky, V., & Tipenko, G. (2008). *Numerical modeling of spatial permafrost dynamics in Alaska* (pp. 1125–1130). Paper presented at Proceedings of the Ninth International Conference on Permafrost, Institute of Northern Engineering, University of Alaska Fairbanks.

MathWorks (2018). MATLAB optimization algorithms. https://www.mathworks.com/help/optim/ug/choosing-the-algorithm.html, Accessed: 2018-01-01.

Meinshausen, M., Smith, S. J., Calvin, K., Daniel, J. S., Kainuma, M. L. T., Lamarque, J.-F., et al. (2011). The RCP greenhouse gas concentrations and their extensions from 1765 to 2300. *Climatic Change*, *109*(1), 213.

Moss, R. H., Babiker, M., Brinkman, S., Calvo, E., Carter, T., Edmonds, J. A., et al. (2008). *Towards new scenarios for analysis of emissions, climate change, impacts, and response strategies* (pp. 1–132). Geneva, Switzerland: Intergovernmental Panel on Climate Change.

Myers-Smith, I. H., Forbes, B. C., Wilmking, M., Hallinger, M., Lantz, T., Blok, D., et al. (2011). Shrub expansion in tundra ecosystems: Dynamics, impacts and research priorities. *Environmental Research Letters*, *6*(4), 45509.

Nicolsky, D. J., Romanovsky, V. E., Panda, S. K., Marchenko, S. S., & Muskett, R. R. (2017). Applicability of the ecosystem type approach to model permafrost dynamics across the Alaska North Slope. *Journal of Geophysical Research: Earth Surface*, *122*, 50–75. https://doi.org/10.1002/2016JF003852

Nicolsky, D. J., Romanovsky, V. E., & Panteleev, G. G. (2009). Estimation of soil thermal properties using in-situ temperature measurements in the active layer and permafrost. *Cold Regions Science and Technology*, *55*(1), 120–129.

Nicolsky, D. J., Romanovsky, V. E., & Tipenko, G. S. (2007). Using in-situ temperature measurements to estimate saturated soil thermal properties by solving a sequence of optimization problems. *The Cryosphere*, *1*(1), 41–58.

Osterkamp, T. E., & Romanovsky, V. E. (1996). Characteristics of changing permafrost temperatures in the Alaskan Arctic, USA. *Arctic and Alpine research*, *28*, 267–273.

Panda, S., Prakash, A., Solie, D., Romanovsky, V., & Jorgenson, T. (2010). Remote sensing and field-based mapping of permafrost distribution along the Alaska Highway corridor, interior Alaska. *Permafrost and Periglacial Processes*, *21*(3), 271–281.

Pastick, N. J., Jorgenson, M. T., Wylie, B. K., Nield, S. J., Johnson, K. D., & Finley, A. O. (2015). Distribution of near-surface permafrost in Alaska: Estimates of present and future conditions. *Remote Sensing of Environment*, *168*, 301–315.

Racine, C., Jandt, R., Meyers, C., & Dennis, J. (2004). Tundra fire and vegetation change along a hillslope on the Seward Peninsula, Alaska, U.S.A. *Arctic, Antarctic, and Alpine Research*, *36*(1), 1–10.

Rawlins, M. A., Nicolsky, D. J., McDonald, K. C., & Romanovsky, V. E. (2013). Simulating soil freeze/thaw dynamics with an improved pan-Arctic water balance model. *Journal of Advances in Modeling Earth Systems*, *5*, 659–675. https://doi.org/10.1002/jame.20045

Riseborough, D. (2010). The mean annual temperature at the top of permafrost, the TTOP model, and the effect of unfrozen water. *Permafrost and Periglacial Processes*, *13*(2), 137–143.

Riseborough, D., Shiklomanov, N., Etzelmller, B., Gruber, S., & Marchenko, S. (2008). Recent advances in permafrost modelling. *Permafrost and Periglacial Processes*, *19*(2), 137–156.

Romanovsky, V., Drozdov, D., Oberman, N., Malkova, G., Kholodov, A., Marchenko, S., et al. (2010). Thermal state of permafrost in Russia. *Permafrost and Periglacial Processes*, *21*(2), 136–155.

Romanovsky, V. E., & Osterkamp, T. E. (1995). Interannual variations of the thermal regime of the active layer and near-surface permafrost in northern Alaska. *Permafrost and Periglacial Processes*, *6*(4), 313–335.

Romanovsky, V., Smith, S., & Christiansen, H. (2010). Permafrost thermal state in the polar Northern Hemisphere during the international polar year 2007–2009: A synthesis. *Permafrost and Periglacial Processes*, *21*(2), 106–116.

Romanovsky, V. E., Smith, S. L., Isaksen, K., Shiklomanov, N. I., Streletskiy, D. A., Kholodov, A. L., et al. (2019). Terrestrial permafrost [in "state of the climate in 2018"]. *Bulletin of the American Meteorological Society*, *99*, 153–159.

Rupp, T. S., Chapin III, F. S. C., & Starfield, A. M. (2001). Response of subarctic vegetation to transient climatic change on the Seward Peninsula in north-west Alaska. *Global Change Biology*, *6*(5), 541–555.

SNAP (2017). Projected monthly and derived temperature products. Fairbanks, Alaska: University of Alaska Fairbanks. http://www.snap.uaf.edu accessed on 08/20/2019.

Sass, J. H., Lachenbruch, A. H., & Munroe, R. J. (1971). Thermal conductivity of rocks from measurements on fragments and its application to heat-flow determinations. *Journal of Geophysical Research*, *76*(14), 3391–3401.

Sazonova, T. S., & Romanovsky, V. E. (2003). A model for regional-scale estimation of temporal and spatial variability of active layer thickness and mean annual ground temperatures. *Permafrost and Periglacial Processes*, *14*(2), 125–139.

Schuur, E. A. G., & Mack, M. C. (2018). Ecological response to permafrost thaw and consequences for local and global ecosystem services. *Annual Review of Ecology, Evolution, and Systematics*, *49*(1), 279–301.

Schuur, E. A. G., McGuire, A. D., Schädel, C., Grosse, G., Harden, J. W., Hayes, D. J., et al. (2015). Climate change and the permafrost carbon feedback. *Nature*, *520*, 171–179.

Shiklomanov, N., Streletskiy, D., Swales, T., & Kokorev, V. (2017). Climate change and stability of urban infrastructure in Russian permafrost regions: Prognostic assessment based on GCM climate projections. *Geographical Review*, *107*(1), 125–142.

Shur, Y. L., & Jorgenson, M. T. (2007). Patterns of permafrost formation and degradation in relation to climate and ecosystems. *Permafrost and Periglacial Processes*, *18*(1), 7–19.

Smith, S. L., Burgess, M. M., Riseborough, D., & Mark Nixon, F. (2005). Recent trends from Canadian permafrost thermal monitoring network sites. *Permafrost and Periglacial Processes*, *16*(1), 19–30. https://doi.org/10.1002/ppp.511

Talbot, S. S., & Meades, W. J. (2011). *Circumboreal Vegetation Map (CBVM): Mapping the green halo concept paper*. Akureyri, Iceland: CAFF International Secretariat. http://hdl.handle.net/11374/209

Vavrek, M. C., Fetcher, N., McGraw, J. B., Shaver, G. R., Chapin III, F. S., & Bovard, B. (1999). Recovery of productivity and species diversity in tussock tundra following disturbance. *Arctic, Antarctic, and Alpine Research*, *31*(3), 254–258.

Verseghy, D. L. (1991). CLASS—A Canadian land surface scheme for GCMs. I. Soil model. *International Journal of Climatology*, *11*(2), 111–133. https://doi.org/10.1002/joc.3370110202

Viereck, L. A. (1970). Forest succession and soil development adjacent to the Chena River in Interior Alaska. *Arctic and Alpine Research*, *2*(1), 1–26.

Viereck, L. A., Dyrness, C. T., Batten, A. R., & Wenzlick, K. J. (1992). The Alaska vegetation classification. Portland, OR: Pacific Northwest Research Station.

Volodin, E. M. (2008). Methane cycle in the INM RAS climate model. *Izvestiya, Atmospheric and Oceanic Physics*, *44*(2), 153–159.

Walker, D. A., Jia, G. J., Epstein, H. E., Raynolds, M. K., Chapin III, F. S. C., Copass, C., et al. (2003). Vegetation-soil-thaw-depth relationships along a low-Arctic bioclimate gradient, Alaska: Synthesis of information from the ATLAS studies. *Permafrost and Periglacial Processes*, *14*(2), 103–123.

Walker, D. A., Raynolds, M. K., Danils, F., Einarsson, E., Elvebakk, A., Gould, W. A., et al. (2005). The Circumpolar Arctic Vegetation Map. *Journal of Vegetation Science*, *16*(3), 267–282.

Walsh, J. E., Chapman, W. L., V, V. E. R., Christensen, J. H., & Stendel, M. (2008). Global climate model performance over Alaska and Greenland. *Journal of Climate*, *21*(23), 6156–6174.

Walvoord, M. A., & Kurylyk, B. L. (2016). Hydrologic impacts of thawing permafrost—A review. *Vadose Zone Journal*, *15*(6), 1–20.

Wang, C., Wang, Z., Kong, Y., Zhang, F., Yang, K., & Zhang, T. (2019). Most of the Northern Hemisphere permafrost remains under climate change. *Scientific Reports volume*, *9*, 3295.

Westermann, S., Østby, T. I., Gisnås, K., Schuler, T. V., & Etzelmüller, B. (2015). A ground temperature map of the North Atlantic permafrost region based on remote sensing and reanalysis data. *The Cryosphere*, *9*(3), 1303–1319.

Woo, M.-K., Kane, D. L., Carey, S. K., & Yang, D. (2008). Progress in permafrost hydrology in the new millennium. *Permafrost and Periglacial Processes*, *19*(2), 237–254.

Wu, X., Nan, Z., Zhao, S., Zhao, L., & Cheng, G. (2018). Spatial modeling of permafrost distribution and properties on the Qinghai-Tibet Plateau. *Permafrost and Periglacial Processes*, *29*(2), 86–99.

Yen, Y.-C. (1981). *Review of thermal properties of snow, ice and sea ice*. Hanover, NH: United States Army Corps of Engineers Cold Regions Research and Engineering Laboratory.

Yershov, E. D., & Williams, P. J. (1998). *General geocryology*, *Studies in Polar Research*. Cambridge, UK: Cambridge University Press. https://books.google.com/books?id = tQBwQgAACAAJ

Yoshikawa, K., & Hinzman, L. D. (2003). Shrinking thermokarst ponds and groundwater dynamics in discontinuous permafrost near Council, Alaska. *Permafrost and Periglacial Processes*, *14*(2), 151–160.

Zhang, Y., Wang, X., Fraser, R., Olthof, I., Chen, W., Mclennan, D., et al. (2013). Modelling and mapping climate change impacts on permafrost at high spatial resolution for an Arctic region with complex terrain. *The Cryosphere*, *7*(4), 1121–1137.